

SURFACE-ENHANCED RAMAN SCATTERING TECHNIQUE FOR NANOPLASTICS DETECTION

Mr. Boonphop Chaisrihwun



A Dissertation Submitted in Partial Fulfillment of the Requirements
for the Degree of Doctor of Philosophy in Petrochemistry and Polymer
Science

Field of Study of Petrochemistry and Polymer Science

FACULTY OF SCIENCE

Chulalongkorn University

Academic Year 2022

Copyright of Chulalongkorn University

เทคนิคเซอร์เฟซเอนฮานซ์รามานสแกตเทอริงสำหรับการตรวจวัดนาโนพลาสติก



วิทยานิพนธ์นี้เป็นส่วนหนึ่งของการศึกษาตามหลักสูตรปริญญาวิทยาศาสตรดุษฎีบัณฑิต
สาขาวิชาปิโตรเคมีและวิทยาศาสตร์พอลิเมอร์ สาขาวิชาปิโตรเคมีและวิทยาศาสตร์พอลิเมอร์

คณะวิทยาศาสตร์ จุฬาลงกรณ์มหาวิทยาลัย

ปีการศึกษา 2565

ลิขสิทธิ์ของจุฬาลงกรณ์มหาวิทยาลัย

Thesis Title SURFACE-ENHANCED RAMAN SCATTERING
TECHNIQUE FOR NANOPLASTICS DETECTION
By Mr. Boonphop Chaisrihwun
Field of Study Petrochemistry and Polymer Science
Thesis Advisor Assistant Professor Dr. Prompong Pienpinijtham

Accepted by the FACULTY OF SCIENCE, Chulalongkorn University in
Partial Fulfillment of the Requirement for the Doctor of Philosophy

..... Dean of the FACULTY OF
SCIENCE
(Professor Dr. POLKIT SANGVANICH)

DISSERTATION COMMITTEE

..... Chairman
(Dr. Suwussa Bamrungsap)
..... Thesis Advisor
(Assistant Professor Dr. Prompong Pienpinijtham)
..... Examiner
(Professor Dr. Voravee Hoven)
..... Examiner
(Associate Professor Dr. SIRILUX POOMPRADUB)
..... Examiner
(Assistant Professor Dr. SUKKANESTE
TUNGASMITA)

จุฬาลงกรณ์มหาวิทยาลัย
CHULALONGKORN UNIVERSITY

บุญภพ ไชยศรีขวัญ : เทคนิคเซอร์เฟซเอนฮานซ์รามานสแกตเทอริงสำหรับการตรวจวัดนาโนพลาสติก. (SURFACE-ENHANCED RAMAN SCATTERING TECHNIQUE FOR NANOPLASTICS DETECTION) อ.ที่ปรึกษาหลัก : ผศ. ดร.พร้อมพงศ์ เพียรพินิจธรรม

การใช้เทคนิคเซอร์เฟซเอนฮานซ์รามานสแกตเทอริง (surface-enhanced Raman scattering, SERS) หาปริมาณอนุภาคระดับนาโนของพลาสติก (nanoplastics, NPLs) นั้น มีข้อจำกัดในเรื่องของขนาดพลาสติกที่แตกต่างกัน ในการศึกษาี้ ได้ประสบความสำเร็จเป็นอย่างมากในการออกแบบวิธีการทดลองเพื่อจัดปัญหาี้ เทคนิค SERS ที่เตรียมได้ช่วยให้สามารถหาปริมาณอนุภาครวมระดับนาโนของพอลิสไตรีน (polystyrene nanospheres, PSNSs) ขนาด 100, 300, 600 และ 800 นาโนเมตร ที่ความเข้มข้นต่ำในตัวอย่างที่เป็นของเหลวหลากหลายชนิดได้ ทั้งนี้การเคลือบอนุภาคทองคำลงบนแผ่นกระจกสไลด์ จะทำให้ได้วัสดุรองรับในการขยายสัญญาณรามาน (SERS substrate) เพื่อใช้เป็นตัวเร่งสัญญาณรามานของพลาสติกให้มากขึ้น โดยการละลาย PSNSs ในสารละลายโทลูอีน (toluene) และเพิ่มความเข้มข้น (preconcentrate) จึงทำให้เทคนิคนี้ประสบความสำเร็จในการหาปริมาณ NPLs ที่มีความเข้มข้นต่ำมาก ๆ ได้ ซึ่งมีขีดจำกัดการตรวจวัด (limit of detection, LOD) เท่ากับ 0.12 ไมโครกรัมต่อมิลลิลิตร นอกจากนี้ยังมีการนำสารหลากหลายชนิด เช่น กลีโกล น้ำตาล กรดอะมิโน และสารซักล้าง มาใช้เป็นตัวกลางในการทดสอบเทคนิคนี้ เพื่อหาผลกระทบของสารรบกวน (interfearfence) นอกจากนี้ เทคนิค SERS ยังมีประสิทธิภาพในการใช้วิเคราะห์เชิงปริมาณของอนุภาค PSNSs ผสม ที่มีขนาดแตกต่างกันคือ 100, 300, 600 และ 800 นาโนเมตร ในอัตราส่วน 1:1:1:1 ในตัวอย่างจริงคือ น้ำประปา น้ำแร่ และน้ำจากแม่น้ำเจ้าพระยา จากการใช้งาน พบว่า เทคนิค SERS ประสบความสำเร็จในการหาปริมาณ PSNSs โดยเฉพาะในช่วงความเข้มข้น 10–40 ไมโครกรัมต่อมิลลิลิตร โดยมี LOD อยู่ที่ 0.32–0.52 ไมโครกรัมต่อมิลลิลิตร

CHULALONGKORN UNIVERSITY

สาขาวิชา ปีโตรเคมีและวิทยาศาสตร์พอลิเมอร์
ปีการศึกษา 2565

ลายมือชื่อนิติต
ลายมือชื่อ อ.ที่ปรึกษาหลัก

6271015023 : MAJOR PETROCHEMISTRY AND POLYMER SCIENCE

KEYWORD Microplastics (MPLs), Nanoplastics (NPLs), Surface-enhanced
D: Raman Scattering (SERS), Polystyrene nanosphere (PSNSs),
Quantification analysis

Boonphop Chaisrihwun : SURFACE-ENHANCED RAMAN
SCATTERING TECHNIQUE FOR NANOPLASTICS DETECTION.
Advisor: Asst. Prof. Dr. Prompong Pienpinijtham

The size-dependent effect of nanoplastics (NPLs) restricts the quantification of NPLs by surface-enhanced Raman scattering (SERS) technique. In this study, we successfully established an innovative preparation method to eliminate this effect. This developed SERS method allowed us to quantify 100-, 300-, 600-, and 800-nm polystyrene nanospheres (PSNSs) in diverse aqueous conditions at a low concentration. The SERS substrate was easily fabricated and used as NPLs signal enhancement with sputtering gold particles onto a glass cover slide. By preconcentrating and dissolving PSNSs in toluene, SERS technique can be successfully quantify NPLs at extremely low concentrations with a limit of detection (LOD) down to 0.12 $\mu\text{g/mL}$. Moreover, the SERS method was also performed in several media such as salts, sugars, amino acids, and detergents in order to investigate the interference effect. Moreover, the SERS method was effectively validated for quantitative analysis of a mixture of 100-, 300-, 600-, and 800-nm PSNSs in a ratio of 1:1:1:1 in real-world media (*i.e.*, tap water, mineral water, and river water). Using our proposed method, the SERS technique successfully approaches the evaluation of PSNSs in the range of 10 to 40 $\mu\text{g/mL}$ with a LOD of down to 0.32–0.52 $\mu\text{g/mL}$.

Field of Study: Petrochemistry and
Polymer Science
Academic 2022
Year:

Student's Signature
.....
Advisor's Signature
.....

ACKNOWLEDGEMENTS

I would like to extend my sincere gratitude to my thesis advisor, Assistant Professor Dr. Prompong Pienpinijtham, for recognizing my potential and granting me the opportunity to pursue a Ph.D. under his guidance. This thesis would not have been possible without his invaluable advice, support, and assistance. He provided me with direction, inspiration, and confidence, which kept me motivated and optimistic throughout my Ph.D. journey.

I would also like to express my appreciation to Professor Dr. Sanong Ekkasit, Associate Professor Dr. Kanet Wongravee, and the Sensor Research Unit (SRU) members for their warm hospitality, comfort, and support during my thesis work. Their presence and assistance were truly invaluable.

I am deeply grateful to Professor Dr. Voravee Hoven, Dr. Suwussa Bamrungsap, Assistant Professor Dr. Sukkaneste Tungasmita, and Associate Professor Dr. Sirilux Poompradub for serving on my thesis committee and providing invaluable feedback and suggestions.

I would like to express my gratitude to Assistant Professor Dr. Natthida Rakkapao and Dr. Harnchana Gatemala for their belief in my capabilities and unwavering support on my chosen path.

I would like to express my profound appreciation to my parents, sisters, and brothers for their unwavering support, understanding, and acceptance of my decisions. Your love and assistance have given me the strength to pursue and achieve my dreams.

Lastly, I would like to acknowledge the Second Century Fund (C2F) and Chulalongkorn University, Thailand, for their financial support. Additionally, this research has also received partial support from the National Nanotechnology Center (NANOTEC), NSTDA, Ministry of Science and Technology, Thailand, through its Research Network NANOTEC (RNN) program.

Boonphop Chaisrikhun

TABLE OF CONTENTS

	Page
ABSTRACT (THAI)	iii
ABSTRACT (ENGLISH)	iv
ACKNOWLEDGEMENTS	v
TABLE OF CONTENTS	vi
LIST OF TABLES	1
LIST OF FIGURES	2
CHAPTER I INTRODUCTION.....	4
1.1. Objective	8
1.2 Scope of the dissertation.....	8
CHAPTER II THEORETICAL BACKGROUND.....	9
2.1 Microplastics and nanoplastics.....	9
2.2 Negative impact of MPLs and NPLs.....	11
2.3 MPLs and NPLs characterization technique	13
2.3.1 Pyr-GC-MS	13
2.3.2 TED-GC-MS.....	14
2.3.3 Infrared spectroscopy	16
2.3.4 Raman microscopy technique (RM).....	17
2.3.4.1 Surfaced enhanced Raman scattering technique (SERS) .	18
2.3.4.2 Detection of NPLs employing SERS.....	22
CHAPTER III MATERIALS AND METHODS	35
3.1 Materials.....	35
3.2 Preparation and characterization of SERS substrate	35
3.3 SERS measurement	36
3.4 Preparation of real-world media samples	36
CHAPTER IV RESULTS AND DISCUSSION	37

4.1. Characterization of SERS substrate	37
4.2. Standard calibration curve for PSNPs with various particle sizes	39
4.3 Effect of interferences	42
4.4 Detection of PSNPs in real-world media	45
CHAPTER V CONCLUSIONS	48
APPENDIX.....	49
REFERENCES	55
VITA.....	69



LIST OF TABLES

Table 1. Summarizes the literature detail of SERS substrate-based metal nanostructured for NPLs detection and identification	23
Table 2. The LODs of previously published SERS approaches compared with our study.	46



LIST OF FIGURES

- Figure 1.** The quantitative analysis process of NPLs in water media using the SERS technique. The PSNSs beads were used to represent NPLs in the environments. SERS detection of PS with different diameters (*i.e.*, 100, 300, 600, and 800 nm) is utilized to demonstrate the elimination of size-dependent effects generated by NPLs with different diameters. 7
- Figure 2.** Jablonski's diagram of quantum energy transitions. (a) Rayleigh scattering, (b) Stokes Raman scattering, and (c) anti-Stokes Raman scattering. 18
- Figure 3.** Schematic drawing of (a) electric field drives localized surface plasmon resonance (LSPR), (b) chemical enhancement mechanism generated by SERS technique, and (c) enhanced Raman scattering of target molecules adsorbed onto the SERS substrate..... 19
- Figure 4** (a) TEM images of PSNSs and PSNSs/AgNPs cluster with their Raman and SERS spectra [57]. (b) schematic of the SERS preparation process using PS NPs and AgNPs in the presence of KI before SERS detection [171]. (c) schematic drawing of SERS detection by drop-casting of NPLs containing AgNPs and MgSO₄ solution on silicon wafer [69]. (d) schematic illustration of the different metal nanostructures exposed to the hotspot for detecting NPLs using the SERS technique [175]......24
- Figure 5.** (a) TEM image of AuNUs/PSNSs cluster and the onset of SERS signal of AuNU: PSNSs (1:1 – 5:1) [66]. (b) schematic of nanowell preparation and SEM image of PSNSs with various diameters on SiO₂PC@Ag and Klarite substrates. (c) SERS spectrum of NPLs on SiO₂PC@Ag and (d) Klarite substrates [60]......27
- Figure 6.** (a) schematic drawing of NPLs detection in the atmospheric environment by Karite substrate utilized mapping technique, and (b) mapping image of NPLs with particle size 360 nm (up) and 500 nm (down) obtained from the mapping area on Karite substrate shown in OM image [56]. (c) schematics drawing of AuNPs@V-shaped AAO substrate fabrication process and (d) SEM image of PSMSs (diameter = 2 μm) on AuNPs@V-shaped AAO substrate in different magnifications [170]. (e) schematic drawing of AuNSs@Ag@AAO substrate preparation and (f) COMSOL simulation of the localized electromagnetic fields of the AuNSs monomer, AuNSs@Ag monomer, and AuNSs@Ag dimer (3D model) and (g) SEM images of 400 nm of PS particles on the SERS substrate with their SERS spectra at different concentrations [58]......29
- Figure 7.** (a) SEM image of Si/MoS₂/Ag substrate with PSNSs with different sizes (*i.e.*, 100, 200, and 300 nm). (b) electric-field distributions in AAO/MoS₂/Ag cavities by employing FDTD simulations. (c) Raman and SERS spectra of AAO/MoS₂/Ag,

Si/MoS₂/Ag, and Si substrate with different sizes of PSNSs. (d) comparison of the SERS intensity ratio of NPLs with different sizes [173].32

Figure 8. (a) schematic illustration of AuNPs decorated sponge to detect MPLs in water and (b) OM images of sponge substrates [174]. (c) schematic illustration of the fabrication of PNPs/RC films and (d) SEM image of 84 nm PSNSs on an AgNWs/RC film [61]. (e) preconcentration and detection of NPLs using membrane filtration and SERS, (f) SEM images of 50 nm standard PSNSs retained on the membrane, and (g) Raman mapping images of 50 nm PSNSs with concentration of 0.1 ng/mL [68]......33

Figure 9. AFM micrographs of the SERS substrate show (a) surface roughness and (b) gold film thickness of the SERS substrate with a 180-second sputtering time. Plots of (c) roughness versus sputtering time, (d) gold film thickness versus sputtering time, and (e) I_{1005} versus gold film thickness. PS latex beads with a diameter of 600 nm were prepared at the concentration of 10 $\mu\text{g/mL}$, for these SERS measurements.....38

Figure 10. (a) OM image and (b) SERS spectra of PS film (i–v) at the edge of, (vi) inside, and (vii) outside the dried droplet. The experiment was carried out using PSNSs with a particle size of 600 nm at a concentration of 10 $\mu\text{g/mL}$40

Figure 11. (a) SERS spectra of PS in the region of 990–1020 cm^{-1} at different PS concentrations, and (b) standard calibration curves of PS with particle sizes of 100, 300, 600, and 800 nm.....42

Figure 12. Schematic drawing for the SERS enhancement area of the substrate. PS films are deposited (a) in and (b) over the enhancement area of the SERS substrate.42

Figure 13. (a) OM image and (b) SERS spectra of PS film prepared from 600-nm PSNSs suspension with SDS interference using our proposed method at different positions.43

Figure 14. I_{1005} of PS films prepared from PSNSs suspensions with various interferences, *i.e.*, NaCl, KCl, MgCl₂, CaCl₂, sucrose, glucose, fructose, arabinose, galactose, SDS, and albumin.44

Figure 15. Plots of I_{1005} against the PS concentration in real-world media, including DI water (control medium), tap water, mineral water, and river water.45

CHAPTER I

INTRODUCTION

Polymer-based plastics are extensively utilized in various applications due to their exceptional properties, such as affordability, lightweight nature, durability, and flexibility [1]. These plastic products have a long lifespan as they are resistant to degradation, typically persisting in the environment for 1 to 50 years after use [2]. The desirable characteristics of plastics lead to high demand for plastic products, resulting in a steady increase in global plastics production. In 2016, the production reached 335 million tons and is estimated to reach approximately 33 billion tons by 2050 [3, 4]. However, only a small percentage of these massive amounts of plastics (6% to 26%) are recycled due to inefficient disposal methods and inadequate waste management systems [5]. Consequently, a significant amount of plastic waste, estimated to be 10,000–40,000 tons, finds its way into the oceans, leading to widespread plastic accumulation across the planet [6]. This accumulation of plastic litter, particularly in marine environments, has had a detrimental impact on aquatic life and human health by generating microplastic particles.[4].

In the natural environment, plastic litter undergoes a gradual deterioration process through physical, chemical, and biological degradation [7-13]. This leads to the fragmentation of plastic waste and the release of a significant amount of microplastics (MPLs) particles [14]. MPLs can be found in various forms, including fibers, fragments, and beads [14-16], and they have been reported as harmful pollutants in soil [17], shorelines [18], freshwater [19], and ocean [9]. The most frequently detected MPLs in freshwater and drinking water are PE, PP, PS, PVC, and PET [16]. The pollution caused by MPLs has adverse effects on a wide range of aquatic habitats, such as plankton [20], algae [21], shrimp [22], and fish [23]. Additionally, MPLs may contain toxins from additives used in industrial manufacturing processes [24, 25]. Their porous and rough surface also makes them prone to attaching persistent organic pollutants (POPs), further enhancing their harmful potential [26]. Consequently, when living organisms ingest these tiny plastic particles, toxins can enter the food chain *via* transfer and bioaccumulation [27]. These MPLs may probably end up in our bodies due to unhealthy seafood and drinking

water consumption [28], which has become a major topic of concern for scientific, public, and political authorities.

MPLs found in the environment can be classified into two main categories: primary and secondary, based on their origin [29]. Primary microplastics (pMPLs) are deliberately produced for commercial purposes, such as microbeads in personal care products (*i.e.*, shower gels, creams, and facial cleansers), synthetic fibers (*i.e.*, nylon), and plastic pellets. After their intended use, these small plastic items can be released into the surrounding environment from industries and households [30, 31]. On the other hand, secondary microplastics (sMPLs) are fragments derived from the accumulation and degradation of larger plastic litter in aquatic ecosystems. They undergo processes like hydrolysis [7, 8], photodegradation [9, 10], thermo oxidations [11], and biodegradation [12, 13]. These processes gradually reduce the molecular weight of the polymer, making it more brittle and resulting in the fragmentation of larger plastic pieces. However, the degradation of plastics does not stop at this stage. Consequently, macroplastics ($> 5 \mu\text{m}$) continue to fragment into MPLs ($5\text{--}1 \mu\text{m}$) [32] and eventually become nanoparticles with diameters ranging from 1000 to 1 nm, which recognize as nanoplastics (NPLs) [33]. It is important to note that NPLs possess a larger specific surface area and greater hydrophobicity compared to MPLs. This characteristic increases their ability to adsorb various hazardous substances from their surrounding environment, posing a threat to organisms that consume them.

The detection of MPLs and NPLs typically involves an initial step of extracting and separating plastic particles from complex matrices, such as water, sand, soil, and living organisms [34]. Subsequently, purification techniques are employed to isolate and purify MPLs and NPLs before proceeding to the analysis stage. Qualitative and quantitative assessments are conducted during analysis based on the distinctive characteristics of MPLs and NPLs [35]. Various chemical approaches, including thermal and vibrational analytical methods, are currently available for the detection of plastic particles. Pyrolysis gas chromatography–mass spectrometry (Pyr-GC–MS) [36, 37] and thermal extraction desorption gas chromatography–mass spectrometry (TED-GC–MS) [38–41] are examples of thermal analytical methods that measure the physical properties of MPLs and NPLs under specific temperature conditions [42]. However, these thermal analytical methods have certain

disadvantages, such as the requirement for sample pre-processing and the potential interference of impurities in the sample, which can affect the accuracy of the analytical results. Furthermore, these techniques involve high reaction temperatures that may cause damage to the analyte present in the sample.

Fourier transform infrared spectroscopy (FTIR) and Raman spectroscopy (RM) are vibrational analytical methods that offer non-destructive identification of polymer types by providing unique chemical fingerprint spectra [43-47]. FTIR is sensitive to water and has limited spatial resolution, making it suitable for detecting plastic particles larger than 20 μm [48]. However, the FTIR method may generate weak signals for small-diameter plastic particles, leading to false negatives or positives, which can pose challenges for quantitative analysis [49]. In contrast, RM is based on the elastic scattering of light and provides information on molecular vibration and rotation, allowing for determining a material's molecular structure [50]. Raman microscopy offers better spatial resolution compared to FTIR, enabling the detection of plastic particles as small as 1 μm [43-46]. Additionally, Raman spectroscopy has advantages such as more straightforward sample preparation, no need for sample staining, and no requirement for specific sample thickness. Nevertheless, using conventional Raman spectroscopy alone, the signal of plastic particles for less than 1 μm is challenging to be detected [51].

Surface-enhanced Raman scattering (SERS) is a sensitive technique for detecting trace amounts of target analytes. It combines Raman spectroscopy with nanotechnology to amplify the Raman signal of the analyte. SERS has been widely employed in various studies to analyze the chemical fingerprint spectra of plastic particles [52-55]. This technique enables the detection of plastic particles smaller than the detection limit of traditional Raman microscopy (approximately 1 μm) [56-62]. The enhancement of the Raman signal in SERS is achieved through the electromagnetic enhancement mechanism, facilitated by plasmonic materials such as silver (Ag), gold (Au), and copper (Cu) nanoparticles (NPs) [63-65]. This mechanism significantly amplifies the signals of nanoplastics (NPLs), allowing them to be detected using standard Raman instruments [56-62]. Consequently, the SERS strategy has proven successful in detecting plastic particles such as PS [57, 58, 66], PP [57], PET [67], and PE [57] in aquatic environments. Recent reports have demonstrated the

detection of NPLs as small as 50 nm in size, with a remarkably low detection limit of 0.1 ng/mL using Raman imaging [68]. However, the size dependence effect has limited the quantitative analysis of NPLs using the SERS technique, resulting in variations in SERS signals at the same concentration due to differences in NPL diameter [56, 57, 59, 69]. This lack of a linear range in relation to the SERS intensity of NPLs hinders the quantitative analysis of NPLs using the SERS method.

To overcome the size-dependent effect of nanoplastics (NPLs) in SERS analysis, this study aims to develop a preparation process that can eliminate this effect and enable the quantitative analysis of NPLs in an aqueous medium. The proposed SERS preparation strategy is depicted in **Figure 1**. Initially, polystyrene nanospheres (PSNSs) of varying sizes are dried in a vacuum chamber at room temperature,

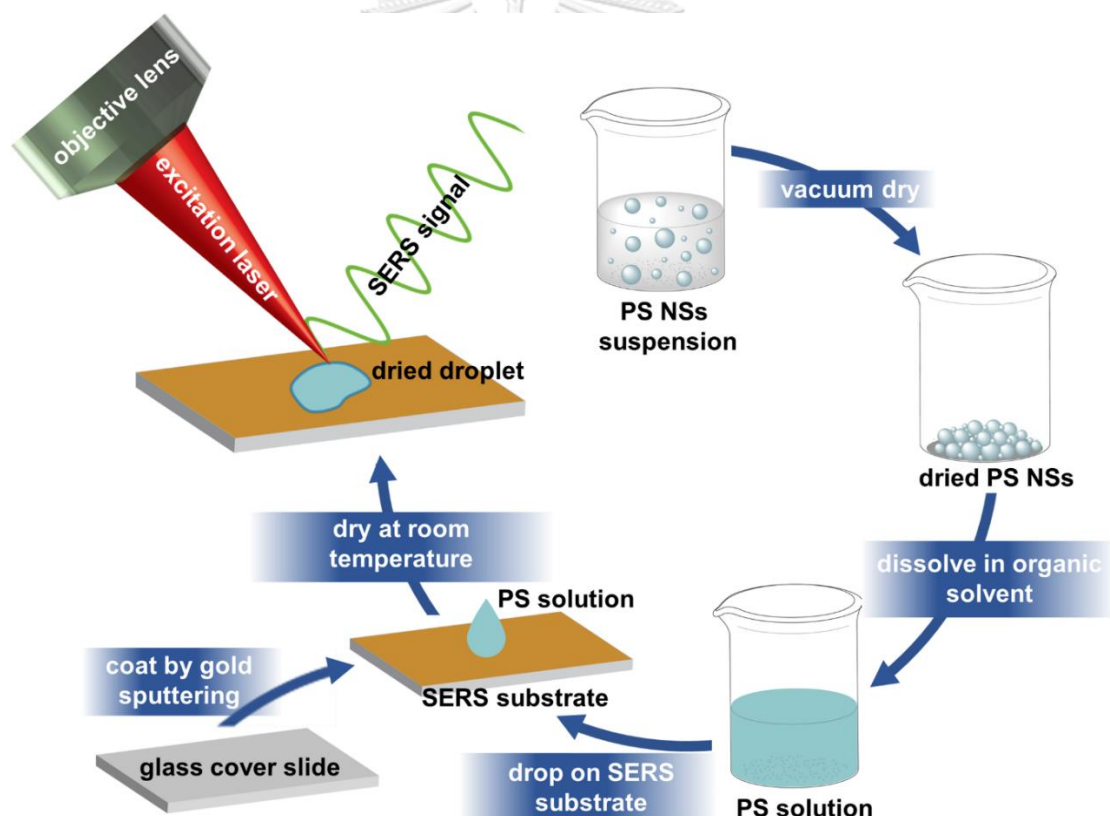


Figure 1. The quantitative analysis process of NPLs in water media using the SERS technique. The PSNSs beads were used to represent NPLs in the environments. SERS detection of PS with different diameters (*i.e.*, 100, 300, 600, and 800 nm) is utilized to demonstrate the elimination of size-dependent effects generated by NPLs with different diameters.

resulting in solid PSNSs. These solid PSNSs are then dissolved in an organic solvent, specifically toluene, to create a PS solution. This step is crucial for eliminating the size-dependence effect of NPLs before conducting SERS measurements. Next, the PS solution is dropped onto a SERS substrate, which is fabricated using gold sputtering equipment and a glass cover slide. During the evaporation of the organic solvent, the PS droplet undergoes a phenomenon known as the coffee-ring effect. This effect causes the PS molecules to migrate from the center of the droplet toward its edge, gradually accumulating at the droplet's border. Apart from eliminating the size-dependence effect, this phenomenon also aids in sample preconcentration, allowing for the quantification of PSNSs in water media even at extremely low concentrations.

Additionally, this study will also examine the effects of different PS particle sizes (*i.e.*, 100, 300, 600, 800 nm), PS concentrations (*i.e.*, 10, 20, 30, 40, 50, 60, and 70 $\mu\text{g/mL}$), interferences (*i.e.*, sugars, salts, amino acids, and detergents), and real-world media (*i.e.*, mineral water, tap water, and Chao Phraya river water).

1.1. Objective

- To develop a facile and sensitive surface-enhanced Raman scattering method to detect the different sizes of nanoplastics in aquatic environments

1.2 Scope of the dissertation

- To perform AFM measurement for characterization of SERS substrate prepared by sputtering gold particles on a glass cover slide using sputtering equipment.
- To exploit the coffee-ring-effect phenomenon for NPLs preconcentration in the preparation step before SERS measurement.
- To investigate the quantitative analysis of different NPLs diameters (*i.e.*, 100, 300, 600, and 800 nm) using the SERS technique and utilize PSNSs as a representative of NPLs in the environments.
- To validate the developed SERS method for quantifying each size of NPLs in 10 individual media (*i.e.*, salts, sugars, proteins, and detergents) and mix size NPLs (*i.e.*, 100, 300, 600, and 800 in the ratio of 1:1:1:1) in the real-world media (*i.e.*, tap water, river water, and mineral water) as the interferences.

CHAPTER II

THEORETICAL BACKGROUND

2.1 Microplastics and nanoplastics

Plastic materials have become essential daily due to their desirable properties such as stability, lightness, affordability, and flexibility. In recent years, the global production of plastic has exceeded 350 million tons, encompassing a wide range of plastics like PET, PC, PP, PE, PS, nylon, and others [70]. When plastic garbages is not correctly handled, its diversity and vast manufacturing have become a concern. As a result, some plastics sink immediately in water, while others float, and some persist for long periods of time. Finally, it degrades into small fragments, leading to adverse ecological impacts [71, 72]. Moreover, plastic degradation in the environment is rather complicated. Several mechanisms may occur during weathering, including the physical, chemical, and biological breakdown of large plastic particles into tiny pieces. They may be broken down into micro (less than 5 mm–1 μm) and nanoscopic sizes (less than 1 μm –1 nm) [73]. It is projected that by 2050, approximately 12,000 million tons of MPLs and NPLs will accumulate on Earth's surface, raising concerns about their potential effects on organisms and human health [74].

Primary plastic particles, such as beads, fibers, and pellets, are intentionally manufactured for specific applications. These plastics can be found in various commercial products, where they exist in micro to nano-sized particles. Additionally, they are released into the environment through industrial processes like abrasives, air blasting, industrial waste, and domestic activities. European cosmetic products, for example, contain plastics as exfoliators in concentrations ranging from 0.05% to 12% by weight. A single use of a cosmetic product (5 mL) can release up to 94,500 polyethylene (PE) particles with sizes ranging from 164 μm to 327 μm [75]. Moreover, NPLs particles (18-66 nm) in quantities of 3×10^{11} have been detected in various cosmetic creams [76], and these particles are also commonly used in medical applications [77]. Synthetic textile microfibers are another significant source of primary plastic particles, with over 1,900 fibers being released in a single washing cycle [78]. Acrylic fabric, polyester-cotton blends, and pure polyester textiles can release up to 138,000, 496,000, and 729,000 fibers, respectively [79]. Surprisingly,

nanoscale 3D printing can release approximately 2×10^{11} residual NPLs particles per minute [80].

Secondary plastic particles are the major source of MPLs and NPLs in the environments. These tiny particles are generated through the fragmentation process of larger plastic products due to various factors such as UV radiation [81, 82], physical abrasion, hydrolysis [83], and biological degradation. This results in lower plastic molecular weight, color changes, and loss of mechanical properties, which degraded the bulk plastics into smaller pieces [81, 82]. Exposure to UV light induces photo-oxidation of the polymer chain, resulting in chain scission and brittleness of the plastic particles [84]. Mechanical stress, such as wave action, abrasion with sand and rocks, and interactions with marine organisms, further contributes to the continuous fragmentation of plastics [82]. UV radiation and oxidative mechanisms play significant roles in plastic degradation [85]. Hydrolysis of plastics occurs when they are submerged in water and undergo condensation cycles, exposure to steam, or contact with high H^+ concentration (acid) or high OH^- concentration (base), accelerating the degradation process. Specific polymers, including nylons, polyester, PET, polycarbonate (PC), and polyurethane (PU), are particularly susceptible to hydrolysis [83]. Biodegradation, driven by microorganisms such as bacteria, fungi, and algae, is another factor that contributes to plastic degradation. During this process, microorganisms colonize the plastic surface and reduce its molecular weight [86, 87]. Enzymatic degradation, facilitated by lipase, proteinase k, and dehydrogenase enzymes attracted to the polymer substrate, followed by hydrolytic cleavages, plays a role in this process [88]. Both natural and synthetic polymers can be degraded by bacteria and fungi [89]. Thermo-oxidative degradation also occurs when plastics undergo slow oxidative breakdown, involving hydrogen abstraction or homolytic scission of carbon-carbon bonds at moderate temperatures, often observed on beaches when exposed to heat [90]. This continuous degradation process generates tiny plastic particles with diameters ranging from micro to nanoscale particles. It has been reported that secondary plastics account for an estimated 97% to 99.9% of the microplastics found in the ocean [91, 92].

2.2 Negative impact of MPLs and NPLs

The presence of microplastics (MPLs) and nanoplastics (NPLs) in the marine environment can have serious consequences for marine pollution, ecological disruption, biodiversity loss, and human health. These plastic particles can enter the ocean through land runoff and sewage treatment plant discharges. Marine organisms can cause physical and chemical harm to their digestive systems when consumed. The impact of these microscopic plastics can disrupt the food chain, starting from smaller organisms and progressing up to larger ones. This can lead to harm and mortality in a wide range of animals, including fish, birds, and marine mammals, ultimately resulting in decreased biodiversity and a negative cascade effect on ecosystem health. MPLs and NPLs have been found in various sources such as drinking water, table salt, seafood, and even the air we breathe. There are concerns about the potential risks to human health, as these particles can be ingested, inhaled, or absorbed through the skin. It is feared that they may cause harm to the digestive and respiratory systems, among other potential health effects. Overall, the presence of MPLs and NPLs in the environment poses significant risks to marine ecosystems, biodiversity, and human well-being, emphasizing the urgent need to address plastic pollution and mitigate its impacts.

Aquatic organisms are being significantly impacted by the accumulation of MPLs and NPLs in their tissues, leading to reduced growth, reproduction, and survival rates. These particles are toxic to various organisms, including microorganisms, crustaceans, shellfish, and sea turtles, as they can be mistaken for food [93]. Previous studies have demonstrated that when plastic combines with hazardous organometallic contaminants, it hampers the growth of microalgae such as *chlorella pyrenoidosa* and *chlorella vulgaris* by increasing oxidative stress and affecting enzyme activity, specifically SOD and catalase [94]. Furthermore, the formation of reactive oxygen species in algae cells elevates cellular oxidative stress, resulting in damage to lipid peroxidation, which negatively impacts algae growth and chlorophyll synthesis [94, 95]. Fish are particularly susceptible to the ingestion and exposure of these toxic plastic particles due to the escalating presence of MPLs and NPLs in aquatic environments [96, 97]. Numerous studies have reported the presence of MPLs in the digestive tracts of various fish, affecting different body parts such as

the skin and gills [98, 99]. Ingestion of MPLs by fish can cause physical injury, structural damage, and even blockages. Consequently, these fish experience changes in feeding behavior, reduced growth rates, and a decline in nutrient absorption rates [100]. Additionally, MPLs have been found to affect the early stages of fish development, leading to reduced mobility and head-to-body length [101]. The presence of MPLs and their additives can cause abnormalities in the cardiovascular system, DNA breakdown, and, ultimately larval death [102, 103].

The consequences of MPLs and NPLs on human health are not yet fully understood, but numerous studies suggest they could be harmful. These particles have been found in seafood, table salt, and beverages, indicating their presence in the human food chain. MPLs and NPLs are small enough to penetrate cell membranes and accumulate in tissues and organs, potentially causing health issues. As humans are at the top of the food chain, we can be exposed to significant amounts of MPLs and NPLs through ingestion, inhalation, and direct skin contact. These particles can accumulate in our bodies and have detrimental effects [104]. Contaminated MPLs present in food, such as polyethylene (PE), polystyrene (PS), polypropylene (PP), polyethylene terephthalate (PET), polyurethane (PU), and polymethyl methacrylate (PMMA), can be consumed by humans and absorbed by the intestines after oral ingestion. They may also be absorbed directly through the intestinal epithelium *via* transcellular and paracellular transport [104, 105]. Additionally, MPLs can cross the skin barrier and be absorbed through the skin when using personal care products, surgical gloves, and prosthetic makeup materials [106]. Prolonged exposure to MPLs can lead to chronic inflammation, cytotoxicity, neurotoxicity, and various neurodegenerative diseases. MPLs can increase oxidative stress in cells by generating reactive oxygen species (ROS) and inducing the secretion of pro-inflammatory factors and cytokines, contributing to neuronal degeneration and potentially leading to diseases such as Alzheimer's [104]. Furthermore, chemicals present in MPLs can sometimes be carcinogenic, increasing the risk of cancer in humans [107]. As a result, several scientists have devised various ways to detect these harmful particles to indicate their danger.

2.3 MPLs and NPLs characterization technique

The detection process for MPLs is typically divided into three steps. Firstly, the MPLs and NPLs are extracted from their surrounding media. Secondly, the extracted particles are separated and purified to obtain relatively pure plastic particles. Finally, the detection involves using analytical techniques that can provide both qualitative and quantitative analysis based on the characteristics of microplastics [34, 108]. This section will focus on quantitatively detecting MPLs and NPLs using various techniques.

MPLs and NPLs detection techniques can be categorized into 2 groups: thermal and vibrational analytical methods. The thermal analytical methods mainly included pyrolysis gas chromatography–mass spectrometry (Pyr-GC–MS) and thermal extraction desorption gas chromatography–mass spectrometry (TED-GC–MS).

2.3.1 Pyr-GC–MS

Pyr-GC–MS is a technique that combines pyrolysis and gas chromatography–mass spectrometry (GC–MS). In this method, the samples are subjected to pyrolysis in an inert environment, and the resulting pyrolysis products are continuously introduced into the GC–MS system to generate a spectrum of the pyrolysis products or programs [38]. By comparing the spectra of the samples with a library of known polymers, this technique can identify the types of plastic particles. Additionally, it provides information on plastic additives, allowing for the analysis of the chemical composition and structural characteristics of the plastic samples. Depending on the number of plastics and the composition of the media, the plastic samples can be analyzed directly [109, 110], or they may require preparation steps such as density separation to remove organic and inorganic materials [111-114]. Since the concentration of plastics in samples is often low, techniques like solvent extraction [115] and pressured liquid extraction (PLE) are used for the preconcentration of plastics [116, 117]. It also included cloud point extraction (CPE) that applies to the preconcentrating of NPLs samples before Pyr-GC–MS analysis [118].

The detection of MPLs and NPLs in various environmental samples using Pyr-GC–MS has been reported in sediments [115, 119], water [112, 120], and biota [120,

121]. This technique has proven effective in identifying different types of MPLs found in marine environments, including PE, PP, PS, PET, PVC, and PA, along with their additives. It can analyze plastic particles as small as 100 μm [122, 123]. The Pyr-GC-MS method can achieve a limit of quantification (LOQ) ranging from 0.1 to 1 μg , depending on plastic sizes and the pyrolysis unit used [124]. The application of this technique to identify and quantify plastics in wastewater after filtration, extraction, and drying provides LOQ around 0.03 μg and 1 μg for PS and PE, respectively [110]. Furthermore, this technique is also used to identify NPLs (PS, 50 nm–1000 nm) in a protocol that combines cross-flow UF, AF, and Pyr-GC-MS [125]. However, it is important to note that analyzing single plastic particles using Pyr-GC-MS can be time-consuming, with each run taking 30–60 minutes or even longer, compared to spectroscopic techniques like μFTIR and Raman microscopy, which can provide results within a couple of minutes or less [126]. Furthermore, Pyr-GC-MS has a limited capacity within the μg -range of the pyrolyzer. Therefore, quantifying environmental samples requires preconcentration steps to increase the concentration of plastics before Pyr-GC-MS analysis. Alternatively, applying the thermo-extraction and desorption (TED) GC-MS technique can allow for analysis of more significant sample amounts in the mg-range [126].

2.3.2 TED-GC-MS

TED-GC-MS, which stands for thermal extraction desorption gas chromatography-mass spectrometry, is a thermal analytical technique that combines thermogravimetric analytical solid phase extraction (TGA-SPE) with thermal desorption gas chromatography-mass spectrometry (TDS-GC-MS). In this method, the plastic sample is first subjected to pyrolysis in a thermogravimetric analyzer under an inert gas. The pyrolyzed products are then absorbed on solid phase reagents for extraction and desorption by increasing the temperature to approximately 600 $^{\circ}\text{C}$. The sample is subsequently separated in the chromatography column and characterized using mass spectrometry (MS). The pyrolysis process in TED-GC-MS generates two ranges of pyrolysis products. The first range (approximately 25–260 $^{\circ}\text{C}$) corresponds to volatile substances, while the second range (above 350 $^{\circ}\text{C}$) corresponds to the characteristic products of the most common polymers. By using TED-GC-MS, the

sample weight can be increased to 100 mg, which allows for analysis with reduced time and potentially overcomes the limitation of reaction tube blockage caused by high molecular weight pyrolysis products, eliminating the need for sample pretreatment. TED-GC-MS was initially applied to analyze environmental samples spiked with PE at a concentration of 1 wt% [40]. Since then, it has been utilized for quantifying different polymer particles in complex environmental matrices from aquatic and terrestrial ecosystems. The quantitative detection achieved with TED-GC-MS provides a limit of quantification (LOQ) values of approximately 10 µg for PE, 1 µg for PP, and 0.2 µg for PS [127].

Furthermore, TED-GC-MS has been utilized to quantify environmental tire wear particles on the streets, revealing that styrene butadiene rubber (SBR), the main component of car tires, can be detected within the range of 3.9 to 9.3 mg/g of the sample [41]. In recent developments, a filtration technique using a smart filter crucible has been introduced as a sampling and detection tool for identifying plastics in beverages. This protocol enables the separation of MPLs, with a size of approximately 5 µm, from the media. The method allows for detecting plastic concentrations as low as 0.01 µg/L and up to 2 µg/L [128].

Compared to Pyr-GC-MS, TED-GC-MS offers a significantly larger sample capacity, approximately 200 times higher. This advantage is beneficial for achieving representativity and sensitivity, although Pyr-GC-MS provides higher detection limits (LOD) and quantification (LOQ) limits. This larger sample capacity allows for the analysis of MPLs in highly polluted samples without sample preparation, even when the polymer content is around 0.5–1 wt% [129]. Whereas the sample-dependent organic matrix can still affect the quantification of the plastic particles by using the entire temperature range (25–650 °C) and losing more thermolabile polymers like PVC when adsorption is cut out below 350 °C [130]. Both Pyr-GC-MS and TED-GC-MS techniques encounter limitations in terms of LODs, particularly when it comes to detecting NPLs. Due to their expected low environmental concentrations (ranging from 1 ng/mL to 1 pg/mL), a preconcentration technique becomes necessary for NPLs detection. Additionally, these thermoanalytical methods are destructive to the samples and can be time-consuming, making them less practical for real-time analysis in environmental systems.

2.3.3 Infrared spectroscopy

FTIR is another commonly used technique for MPLs analysis. It belongs to the category of vibrational spectroscopic techniques that exploit the excitation of vibrational transitions by infrared light, generating a unique fingerprint spectrum for each type of plastic. This spectrum can then be used to identify and distinguish different types of MPLs particles. FTIR can be applied in two different modes of operation. The first mode is attenuated total reflection FTIR (ATR-FTIR), which is typically used for MPLs with particle sizes larger than 500 μm [45]. The second mode is focal plane array (FPA) detector-based micro-FTIR (FPA- μFTIR), which enables the imaging of MPLs particles on filters with a resolution of approximately 10–20 μm [44, 45]. It is important to note that FTIR can only be applied to analyze bulk plastics, as its limit of LOQ is typically 10 μm or higher [43-45, 131]. Nevertheless, this technique has been successfully used to identify and characterize MPLs particles in various environmental samples, including water [132-134] and terrestrial environment [135, 136], air pollution [137, 138], food [111, 139], and drinking water [140, 141].

μFTIR spectroscopy (μFTIR) is an FTIR-based method used to analyze plastic particles lower than 500 μm . This technique uses an FTIR spectrometer with an optical microscope (OM). μFTIR can be employed for analyzing preselected plastic particles or the entire filter area through chemical imaging. Preselection of particles before IR measurement can be done manually [132] or automatically using optical images [142]. FTIR imaging can measure all MPLs particles within the analyzed area. However, analyzing a large area can be time-consuming due to the high number of spectra that need to be measured and processed. Therefore, the collection area is often restricted to a subarea on the filter. This technique has successfully quantified and identified MPLs in water and complex wastewater samples. The theoretical limit for detecting small particles using μFTIR spectroscopy ranges from about 1.7 μm at 4000 cm^{-1} to 13 μm at 500 cm^{-1} [143]. This means that μFTIR can efficiently detect and identify particles larger than 10 μm [144, 145] or 20 μm [146, 147]. Due to this limitation, Raman microscopic (RM) techniques have an advantage over FTIR imaging, especially for detecting plastic particles with a diameter lower than 10 μm .

2.3.4 Raman microscopy technique (RM)

Raman spectroscopy is a light scattering technique that is based on the Raman effect, which occurs when the frequency of the scattered light differs from the frequency of the incident light [148]. This technique is widely used for quantitative and qualitative analysis of various materials. Raman spectroscopy offers excellent versatility in terms of sampling procedures, making it applicable in various scientific fields. It requires minimal sample preparation and can analyze materials with low concentrations [149]. Furthermore, Raman spectroscopy provides a fingerprint region of the molecules, allowing for the identification and characterization of the chemical structures of materials [150].

Raman spectroscopy exploits the Raman scattering effect of molecules originating from light-molecule interaction. When the laser (monochromatic light) is beamed onto the molecules, the molecules are excited into the virtual energy stage (extremely unstable), as illustrated in **Figure 2**, from which the scattered photons are emitted instantly (returns to the lower energy stage). Most scattered photons are emitted with the same energy as a photon in the incident one (Rayleigh scattering, **Figure 2a**). However, some scattered photons can be emitted with energy lower or higher than the photon in the incident light, corresponding to Stokes Raman scattering (**Figure 2b**) and anti-Stokes Raman scattering (**Figure 2c**). The difference in energy between the inelastic Raman scattered photon and the incident photon corresponded to the vibrational peak shown in the Raman spectrum [48, 151, 152].

Raman microscopy combines the principles of Raman spectroscopy and optical microscopy, making it a powerful technique for detecting and identifying MPLs. It allows scientists to investigate MPLs by focusing a laser beam onto plastic particles and obtaining a Raman spectrum. Each type of MPLs exhibits a unique set of vibrational modes in its Raman spectrum, enabling differentiation between different types of MPLs and mixtures of components such as additives and pigments. However, conventional Raman microscopy faces challenges when detecting and identifying plastic particles smaller than 1 μm . This is primarily due to the intrinsic low scattering efficiency of Raman spectroscopy ($d\sigma_{\text{R}}/d\Omega \sim 10^{-31}\text{cm}^2.\text{sr}^{-1}$) [153] and the diffraction limit of a light source [154]. This reason results in a lack of data about NPLs in the environments.

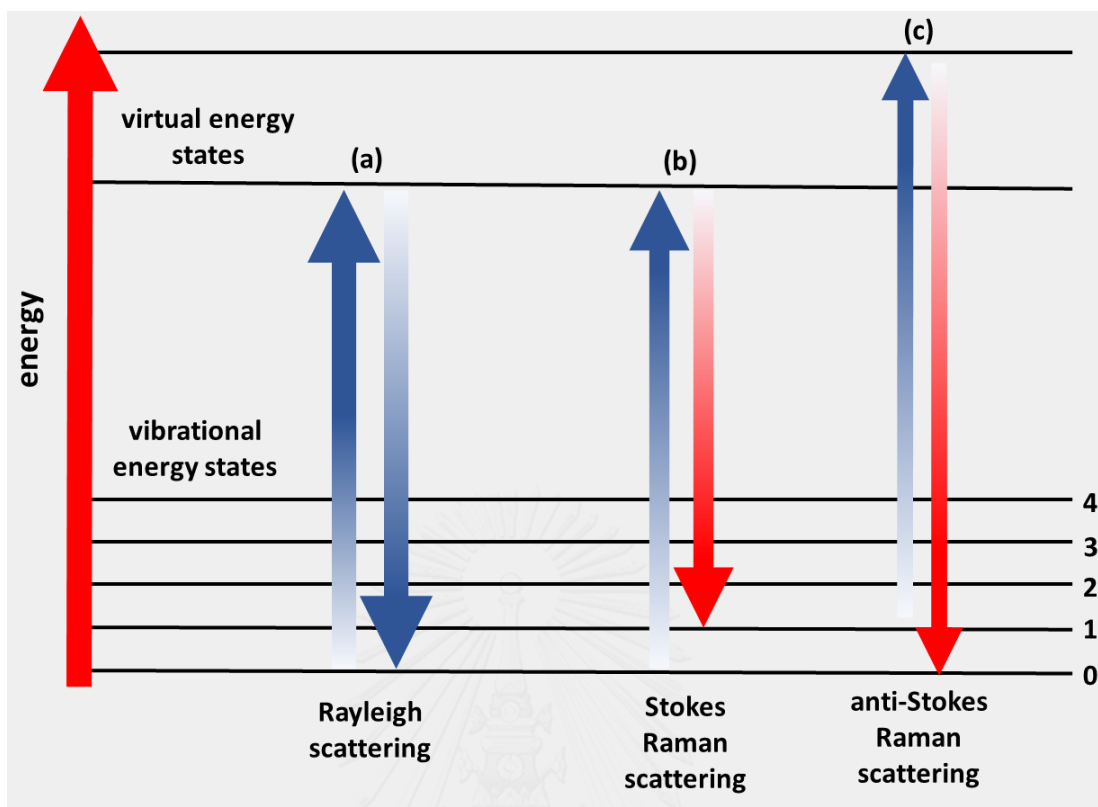


Figure 2. Jablonski's diagram of quantum energy transitions. (a) Rayleigh scattering, (b) Stokes Raman scattering, and (c) anti-Stokes Raman scattering.

2.3.4.1 Surfaced enhanced Raman scattering technique (SERS)

To overcome the limitations of traditional Raman microscopy, surface-enhanced Raman spectroscopy (SERS) has been developed. SERS is an ultra-sensitive technique that can detect single molecules, providing molecular fingerprints for target analyte identification [8, 9]. In addition, this technique can measure the molecules adsorbed on the metal surfaces and increase the Raman signal of an analyte. This enhanced Raman signal is achieved through improved electric field enhancement *via* surface plasmon resonance (SPR) in metallic nanostructures such as gold (Au), silver (Ag), and copper (Cu) [155]. SERS operates through two main mechanisms: electromagnetic enhancement and chemical enhancement. Electromagnetic enhancement occurs when the incident light drives the conducting electrons on the surfaces of metal nanoparticles. This induces localized surface plasmon resonance (LSPR), where the electrons oscillate coherently with the frequency of the incoming light, generating an electromagnetic field around the interface of the metal NPs, as shown in

Figure 3a. The electromagnetic enhancement is more pronounced near the metal surface. This phenomenon greatly amplifies the Raman signal of analytes (enhancement factor of approximately 10^{14} – 10^{15}) [156] and plays a crucial role in achieving high SERS sensitivity [157].

In the same way, the spatial location of a target molecule directly influences the Raman scattering signal, particularly at the hot spot between the interfaces of NPs. The SERS activity of the adsorbed molecules at the hot spot is significantly different from other regions. The enhancement effect diminishes rapidly as the molecules are positioned further away from the hot spot [157]. The chemical enhancement mechanism involves the interaction of target molecules with the metal NP substrates. This interaction can lead to chemical complexation or charge transfer, causing changes in the Raman polarizability of the molecules. This chemical enhancement provides an enhancement factor of 10^1 – 10^2 (**Figure 3b**) [158]. In the case of ordinary Raman, its intensity is dependent on molecular polarization (P_0), and the magnitude of P_0 (Raman-shifted frequency: ω_R), which is mainly controlled by the polarization rate of molecular

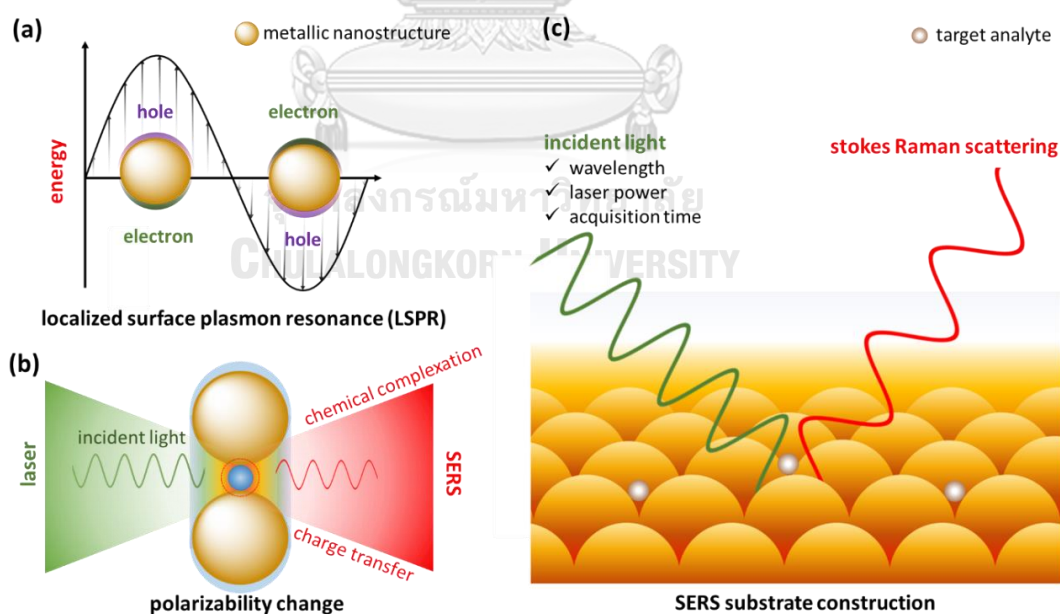


Figure 3. Schematic drawing of (a) electric field drives localized surface plasmon resonance (LSPR), (b) chemical enhancement mechanism generated by SERS technique, and (c) enhanced Raman scattering of target molecules adsorbed onto the SERS substrate.

electrons (α_0^R) and the intensity of incident electromagnetic radiation E_0 (frequency: ω_0) [158] as shown in the formula: $P_0(\omega_R) = \alpha_0^R(\omega_0, \omega_R)E_0(\omega_0)$. Under the SERS condition, Raman dipole (P) is dependent on the modified Raman polarizability (α^R) and the enhanced local electromagnetic field (E_{loc}) around the surface of the metal NPs under the combined effect of electromagnetic and chemical mechanisms as shown in the formula: $P(\omega_R) = \alpha^R(\omega_0, \omega_R)E_{loc}(\omega_0)$.

The application of SERS is necessary to understand its mechanism to control and maximize the SERS signal for practical detection (**Figure 3c**), which is categorized into three main factors as will be discussed as follows;

The first factor represents the incident electromagnetic radiation is a crucial factor in SERS, and several setup parameters must be adjusted for optimal performance. These parameters include the excitation wavelength, laser power, and acquisition time [159]. The Raman scattering efficiency can be influenced by the laser wavelength, as the intensity is inversely proportional to the fourth power of the excitation wavelength (λ) [126]. Depending on the desired application, the excitation wavelength can be selected from a wide range, from ultraviolet to near-infrared. To maximize Raman signal amplification, the laser wavelength should be chosen to match the localized surface plasmon resonance (LSPR) extinction maximum (λ_{max}) of the substrate, which results in the maximum enhancement of the Raman signal [160]. Additionally, the laser wavelength should be selected to minimize fluorescence interference and, in some cases, a lower-power, longer-wavelength laser (*e.g.*, 785 nm) may be preferred to detect specific vibrational modes, such as C–H stretching vibrations in polymers like PE, PP, and PVC [126]. The 532 nm excitation laser is often chosen to observe C–H stretching vibrations more effectively. In practice, the SERS signal intensity can be increased by extending the acquisition time and using higher laser power. However, it is important to consider that higher laser power and longer acquisition times can potentially damage or burn the samples. Therefore, suitable laser power and acquisition time should be carefully adjusted before conducting measurements to ensure optimal signal enhancement without sample damage.

The characteristics of the target molecule constitute the second factor to consider in SERS. In a typical scenario, the Raman intensity is determined by the

Raman scattering cross-section of the target molecules, which is the signal intensity ratio to the incident power density. The polarizability of the electron cloud within the molecules, which reflects its ability to deform in the presence of an electric field, is closely related to the Raman scattering cross-section. Molecules that can undergo polarization (*i.e.*, shape, size, and direction changes during vibration) are classified as Raman-active molecules [161]. The degree of polarizability of the target molecules primarily influences their Raman scattering cross-section. Molecules with electron-rich functional groups and an extended π - π system tend to exhibit large Raman cross-sections (β). For example, the Raman cross-section of cyclohexane is $5.2 \times 10^{-30} \text{ cm}^2 \cdot \text{sr}^{-1} \cdot \text{mol}^{-1}$, while that of benzene is $2.9 \times 10^{-29} \text{ cm}^2 \cdot \text{sr}^{-1} \cdot \text{mol}^{-1}$ [162]. Consequently, polymers like PS produce higher Raman intensity compared to PE and PP when their diameters are the same.

The third factor to consider in SERS is the design of the SERS substrate surface. The electromagnetic (EM) enhancement activity is directly influenced by the engineering of the metal nanostructure and the choice of materials for the SERS substrate. The selection of substrate materials depends on their ability to exhibit plasmonic excitonic activity at the excitation wavelength. Metal nanostructures such as gold (Au), silver (Ag), and copper (Cu) are known to support light-excited surface plasmons and offer excellent SERS enhancement capabilities. Ag NPs, for example, exhibit plasmon resonances in the visible and near-infrared regions, while Au and Cu NPs are often used to excite plasmons in the infrared and near-infrared regions [163]. Additionally, semiconductors and dielectric materials with high stability can also be used to construct SERS substrates. However, their SERS enhancement capabilities are generally limited [164-166]. A plasmonic nanostructure with a high hot spot density could create a high amplification of SERS. The enhancement factor (EF), which is determined using the equation below, is the fundamental metric for evaluating the SERS substrate performance;

$$EF = \frac{I_{\text{SERS}}/N_{\text{SERS}}}{I_{\text{RS}}/N_{\text{RS}}}$$

Where I_{RS} and I_{SERS} are the ordinary Raman intensity and SERS intensity, and N_{RS} and N_{SERS} are the numbers of molecule analytes by ordinary Raman and SERS.

The SERS technique offers significant advantages in detecting and identifying small numbers of analytes, including single molecules, by effectively enhancing their Raman signals. As a result, this technique can be particularly useful in detecting and identifying tiny plastic particles, especially those with sizes smaller than 1 μm or NPLs with weaker Raman intensity.

Based on the information provided earlier, the SERS technique holds great potential for the detection of NPLs that are smaller than the detection limit of conventional Raman spectroscopy [49, 56, 57, 69, 154]. By utilizing engineered metallic nanoparticle substrates, the SERS technique can greatly enhance the Raman signal of tiny plastic particles in close proximity to the metal interface. With this principle in mind, we can expect that the detection and identification of MNPLs, particularly those with sizes smaller than 1 μm and at low concentrations, can be achieved by applying SERS.

2.3.4.2 Detection of NPLs employing SERS

Detecting NPLs using the SERS technique and optimizing the plasmonic hotspots for achieving a high SERS enhancement factor present significant challenges. In this regard, substrates composed of nanoparticles with sharp edges, such as nanocubes and nanostars, have shown effectiveness in enhancing the scattering signal compared to spherical nanoparticles or aggregates [167, 168]. Optimizing the laser power is also crucial for NPL analysis since the temperature around the hotspots can reach up to 200 $^{\circ}\text{C}$ [169], exceeding the glass transition temperature (T_g) of the most common plastics. Such high temperatures can lead to variations in peak intensity and alterations in the physical properties of NPL particles. Hence, optimizing both laser wavelengths and power is necessary [167]. It is worth mentioning that the application of the SERS technique in the field of NPL detection is still in its early stages. Current research in this area is summarized in **Table 1**.

Because the fabrication of a SERS hot spot is a possible way to detect NPLs, many scientists have developed a novel method to create hotspots for NPLs signal amplification based on novel SERS substrates.

Table 1. Summarizes the literature detail of SERS substrate-based metal nanostructured for NPLs detection and identification

SERS substrate	type of NPLs	lowest LOD	detection range	ref.
AgNPs colloid	PS (100 and 500 nm), PP, and PE (10 μ m)	40 μ g/mL	+ good EF – not suitable for actual environmental samples – applicable to PS only	[57]
Krarite substrates	PS (360 nm, 500 nm, 1 μ m, 2 μ m, and 5 μ m) and PMMA (360 nm, 500 nm, 2 μ m, and 5 μ m)	26 μ g/mL	+ real atmospheric samples + good sensitivity – commercial substrate is not cost-effective – low EF	[56]
AgNWs/RC film	PS (84 and 630 nm)	100 μ g/mL	+ low cost and flexible – high LODs, and low EF	[61]
AuNPs@V-shaped AAO SERS substrate	PS (1, 2, and 5 μ m) and PMMA (1 and 2 μ m)	26 μ g/mL	+ potentially scale up and low-cost – low sensitivity, complex composition induce fluorescence and low EF	[170]
Gold nanourchins	PS (600 nm)	83 μ g/mL	+ good sensitivity – not suitable for real environmental samples – applicable to PS only	[66]
Ag nanowire membrane	PS (50, 100, 300, 500, and 1000 nm) and PMMA (500 nm)	0.1 ng/mL	+ pre-concentration of the sample, low cost, real sample analysis, and good sensitivity with high EF – low EF for large NPLs	[68]
Ag nanoparticles	PS (50, 100, 200, and 500 nm)	6.25 μ g/mL	+ simple method and real sample analysis + good detection range and quantification with recovery studies – high LODs	[171]
spherical gold nanoparticles	PS (161 and 33 nm) and PET (62 nm)	10 μ g/mL	+ rapid, simple, and effective methodology – high LODs and low reproducibility – high concentration required of analyte	[67]
SiO ₂ PC@Ag	PS (100, 200, 500, 800, and 1000 nm)	5 μ g/mL	+ better than Klarite, low LODs, and good linear response – the same shape of nanoplastics used	[60]
AuNPs	PS (500 nm 1, 5 nm) and PMMA (300 and 1000 nm)	250 μ g/mL	+ a rapid and simple method and real sample analysis – optimization of parameters + size variation in nanoplastics is lacking + simple detection of PS up to 50 nm	[172]
AgNPs	PS (50 nm)	200 μ g/mL	+ use of automated Raman mapping – no quantification or other studies	[69]
AuNSs@Ag@AAO substrates	PS (400, 800, 2300, 4800 nm)	50 μ g/mL	+ good sensitivity for smaller size nanoplastics, real water sample analysis and no effect of natural organic matter – not good for larger-size nanoplastic – same shape of nanoplastic used + use of hotspot engineering	[58]
Anodic Aluminum Oxide/MoS ₂ /AgNPs	PS (100, 200, 300 nm)	-	+ good for small-size nanoplastics – commercial substrate and no-real sample analysis – focus on spherical shape nanoplastic only + highly flexible substrate and qualitative and quantitative information for single analysis	[173]
gold nanopore	PMMA (10 nm)	500 μ g/mL	– no-real sample analysis and methodology is quite complex + qualitative and quantitative analysis	[62]
Gold-modified sponge substrates	PS, PET, PE, PVC, PP, and PC (80-150 μ m)	100 μ g/mL	+ various plastic types used + real-world sample analysis – high volume of samples required	[174]

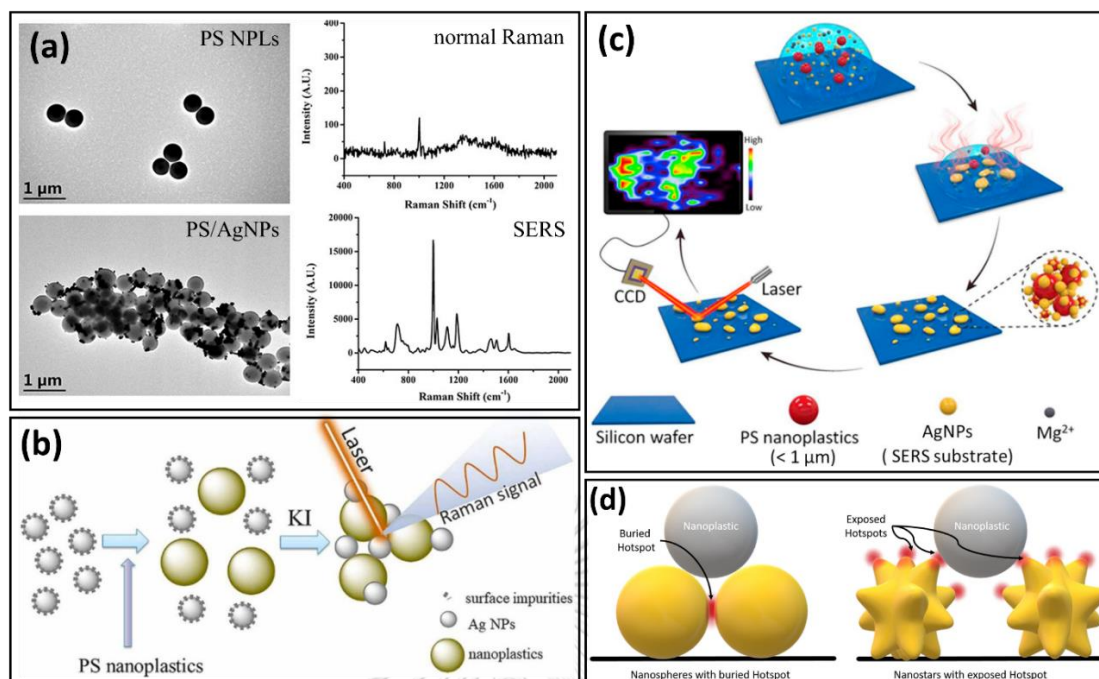


Figure 4 (a) TEM images of PSNSs and PSNSs/AgNPs cluster with their Raman and SERS spectra [57]. (b) schematic of the SERS preparation process using PS NPs and AgNPs in the presence of KI before SERS detection [171]. (c) schematic drawing of SERS detection by drop-casting of NPLs containing AgNPs and MgSO₄ solution on silicon wafer [69]. (d) schematic illustration of the different metal nanostructures exposed to the hotspot for detecting NPLs using the SERS technique [175].

Lv *et al.* [57] conducted a study where inorganic salts, specifically NaCl, were used to facilitate the aggregation of NPLs and enhance interparticle contact, generating numerous SERS hotspots. This method successfully determines the chemical composition of PSNSs in aqueous solutions. In the experiment, SERS substrates based on AgNPs were synthesized in the laboratory and mixed with PS, PE, and PP particles to enhance their Raman signal. NaCl was also introduced to the mixture of plastics and AgNPs to induce aggregation and the formation of clusters, which in turn provided a large number of SERS hotspots to amplify the Raman signal of the plastics. The PSNSs/AgNPs cluster demonstrated significant SERS activity compared to PSNSs alone (**Figure 4a**), allowing this approach to detect 100 nm plastic particles down to 40 µg/mL with an enhancement factor of about 4×10^4 .

Furthermore, Hu *et al.* [171] conducted a similar approach to detect NPLs in a solution by utilizing potassium iodide (KI) as an aggregating agent for AgNPs and as

a cleaner for surface impurities (**Figure 4b**). In this study, NPLs with particle sizes ranging from 50 nm–500 nm are individually mixed with AgNPs solution and KI to generate NPLs/AgNPLs clusters before measuring the SERS signal. The detection of NPLs by this method was proven to be sensitive, efficient, and highly repeatable with low influence from interfering agents, effectively used to discriminate 100 nm of PSNSs as low as 6.25 $\mu\text{g/mL}$ in pure water.

Later, Zhou *et al.* [69] developed a SERS substrate utilizing AgNPs to detect PSNSs in the presence of MgSO_4 using the SERS mapping technique. The detection of NPLs in a dry stage was achieved by drop-casting an aqueous mixture of PSNSs, AgNPs, and MgSO_4 onto a silicon wafer. The presence of MgSO_4 in the droplet facilitated the rapid and dense reuniting of AgNPs and PSNSs on the silicon wafer during water evaporation, allowing for direct mapping of the dry droplet (**Figure 4c**). This method enabled the detection of PSNSs as small as 50 nm, with a limit of detection (LOD) of approximately 5 $\mu\text{g/mL}$ for river water spiked samples. However, the technique suffers from limitations in terms of reproducibility and its applicability to other types of NPLs, such as PE, PP, and PVP.

In contrast to the method developed by Caldwell *et al.* [59], a different approach was employed in this study. A solution of AuNPs was prepared and applied to soak a glass cover slide, ensuring a uniform distribution of AuNPs on the surface. Subsequently, PS and PET NPLs suspensions were dropped onto this SERS substrate. The SERS signal of NPLs was measured at the edge of the dry droplet, where a higher concentration of NPLs is typically observed (*i.e.*, drop edges, particle aggregates, or drying clusters). Using this SERS methodology, PS and PET particles could be detected at concentrations as low as 10 $\mu\text{g/mL}$ and 15 $\mu\text{g/mL}$, respectively, with an enhancement factor of up to 446. However, it is worth noting that the limit of detection for NPLs in this study remains relatively high compared to environmental samples, estimated to be in the range of 1 ng/mL to 1 pg/mL.

According to the previous study, using spherical metallic nanostructures and aggregates to detect plastic particles can pose challenges in achieving effective plasmonic hotspots (**Figure 4d**). The difference in size between the NPLs and the metal nanostructures makes it difficult for the NPLs to come into proximity with the hotspots, limiting the SERS effect. To address this issue, Lee *et al.* [8], synthesized

gold nanourchins (urchin-shaped NPs with irregular spikes around the core: AuNUs) and employed them as a SERS substrate. A solution containing NPLs and AuNUs was drop-casted onto aluminum foil, resulting in the aggregation of the AuNUs around the NPLs particles, facilitating SERS enhancement (**Figure 5a**). As a result, NPLs with a diameter of 600 nm can be effectively detected and identified by this SERS technique.

Chang *et al.* [60] developed a novel nanowell SERS substrate consisting of self-assembled SiO₂ particles coated with silver films (SiO₂PC@Ag). The substrate was created using an interfacial assembly method to fabricate opal-structured assemblies of SiO₂ nanospheres. A thin layer of AgNPs was sputtered onto the SiO₂ nanospheres to achieve the SERS effect. Due to the coffee ring effect, when NPLs were drop-casted onto the substrate, they would position themselves within the nanowells, as depicted in **Figure 5b**, facilitating data acquisition. The SiO₂PC@Ag substrate exhibited higher sensitivity for NPLs detection compared to the commercial Karite substrate (**Figure 5c** compared to **Figure 5d**). Moreover, single PSNSs with particle sizes as small as 200 nm in deionized water could be detected at concentrations as low as 0.5 µg/mL. However, in the case of complex environmental samples such as bottled water, tap water, and river water, the presence of interfering substances increased the limit of detection (LOD) to 5 µg/mL.

Because hotspots play a significant role in the SERS detection of NPLs, researchers try to create the metal nanostructure to dominate orderliness and stability. On the other hand, the organized structure may link theoretical simulation with observable data. Highly ordered metal nanostructure arrays enable NPLs detection and even Raman imaging of individual nanoplastics. Xu *et al.* [56] developed a system using a commercial Karite substrate (**Figure 6a**) consisting of a dense grid of gold-inverted pyramidal cavities. These cavities act as hotspots that amplify the Raman signal of the sample, improving detection sensitivity. The drop-casting technique was employed to evaluate the SERS signal of the Karite substrate when NPLs were present. However, due to the small size of NPLs (less than 500 nm), it becomes challenging to locate and collect data from individual particles using a Raman microscope. To overcome this challenge, Raman imaging was utilized to rapidly detect NPLs on the Karite substrate at random positions without prior knowledge of their locations (**Figure 6b**).

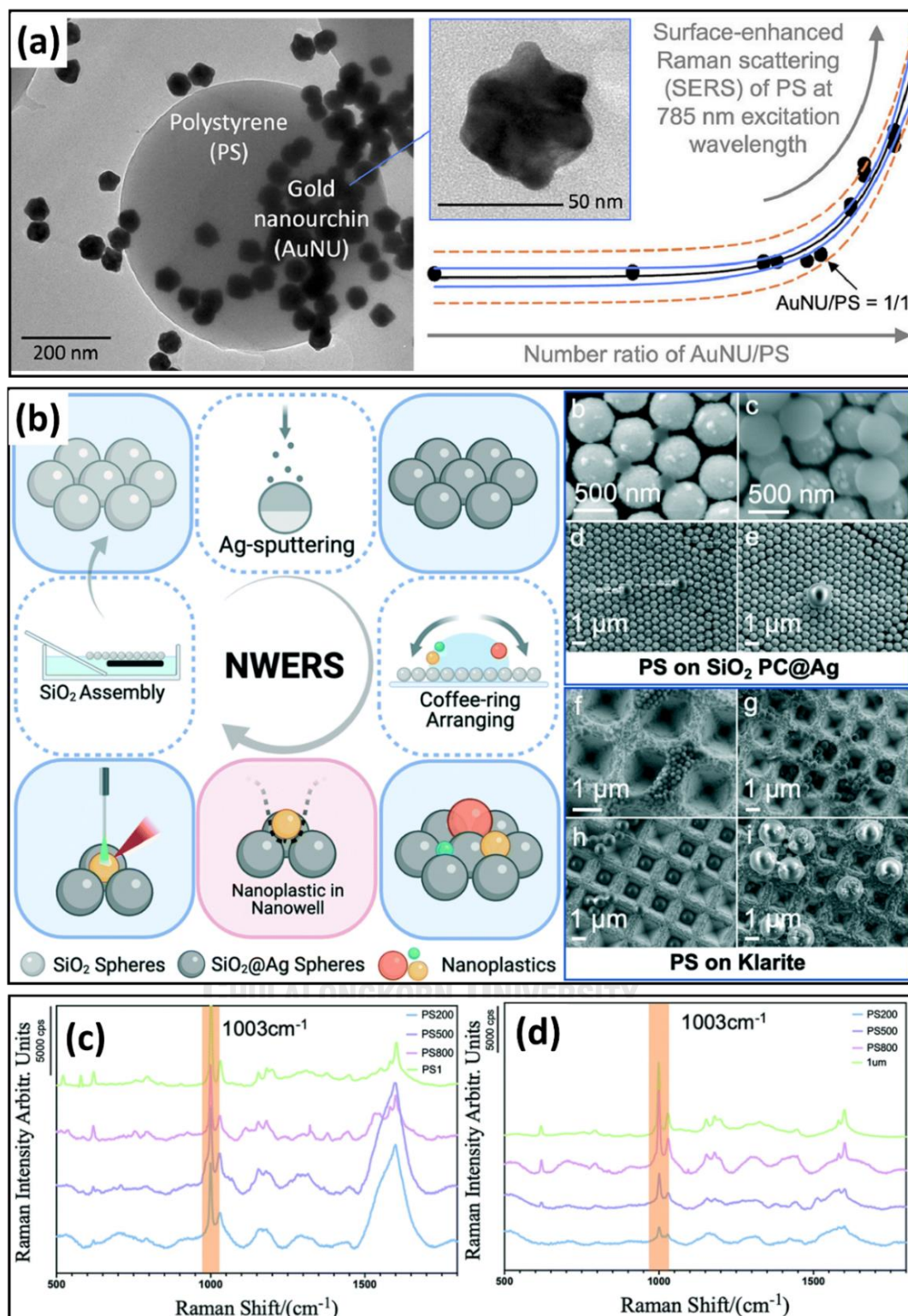


Figure 5. (a) TEM image of AuNUs/PSNs cluster and the onset of SERS signal of AuNU: PSNs (1:1 – 5:1) [66]. (b) schematic of nanowell preparation and SEM image of PSNs with various diameters on SiO₂PC@Ag and Klarite substrates. (c) SERS spectrum of NPLs on SiO₂PC@Ag and (d) Klarite substrates [60].

This approach successfully mapped NPLs with particle sizes as small as 360 nm under ideal conditions and 460 nm when isolated from ambient airborne particles.

Liu *et al.* [170] developed a SERS substrate using V-shaped nanopores fabricated from anodized aluminum oxide (AAO). The AAO template was then sputtered with AuNPs to create an AuNPs@V-shaped AAO SERS substrate (**Figure 6c**). NPLs were drop-casted onto the substrate, and data were acquired from individual plastic particles on the substrate, as shown in the SEM image (**Figure 6d**). This SERS substrate enabled the detection of MPLs with particle sizes of 2 μm and 5 μm . However, detecting nano-sized plastic particles using this approach remains challenging. Compared to the standard Karite substrate, which shares a similar inverted-cone nanostructure and metal NPs, the Karite substrate outperformed the AuNPs@V-shaped AAO substrate in SERS performance. This is attributed to the larger average top diameter of the Karite substrate (1.5 μm) compared to the V-shaped AAO nanopores (400 nm), allowing for better accessibility of particles to the regions of the strongest electric field. Another reason is that the deposition of metal NPs on the AAO structure may lead to disordered deposition and random aggregation of metal NPs, which hinders the ordered structure from plasmonic coupling effects. Nevertheless, the proposed AuNPs@V-shaped AAO SERS substrate offers a cost-effective solution for the large-scale detection of MPLs.

Similar to the previous study, Le *et al.* [58] fabricated V-shaped nanopores in an AAO template and inserted silver-coated gold nanostars (AuNSs@Ag) into the pits to enhance the detection of MPLs (**Figure 6e**). The AuNSs exhibited a highly localized electric field intensity concentrated near the tip region of the nanostar spikes. The formation of dimer structures within the AAO pore further enhanced the electric field intensity at the nanogap, as depicted in **Figure 6f**. Moreover, the coating of Ag on AuNSs significantly improves the electric-field density by a factor of 3. This provides AuNSs@Ag@AAO substrate yields the strongest SERS signal of NPLs due to the plasmonic of AuNSs@Ag@AAO substrates can be resonant well with NPLs materials, resulting in the significant enhanced of PSNSs signal of 400 nm down to 50 $\mu\text{g/mL}$. (**Figure 6g**).

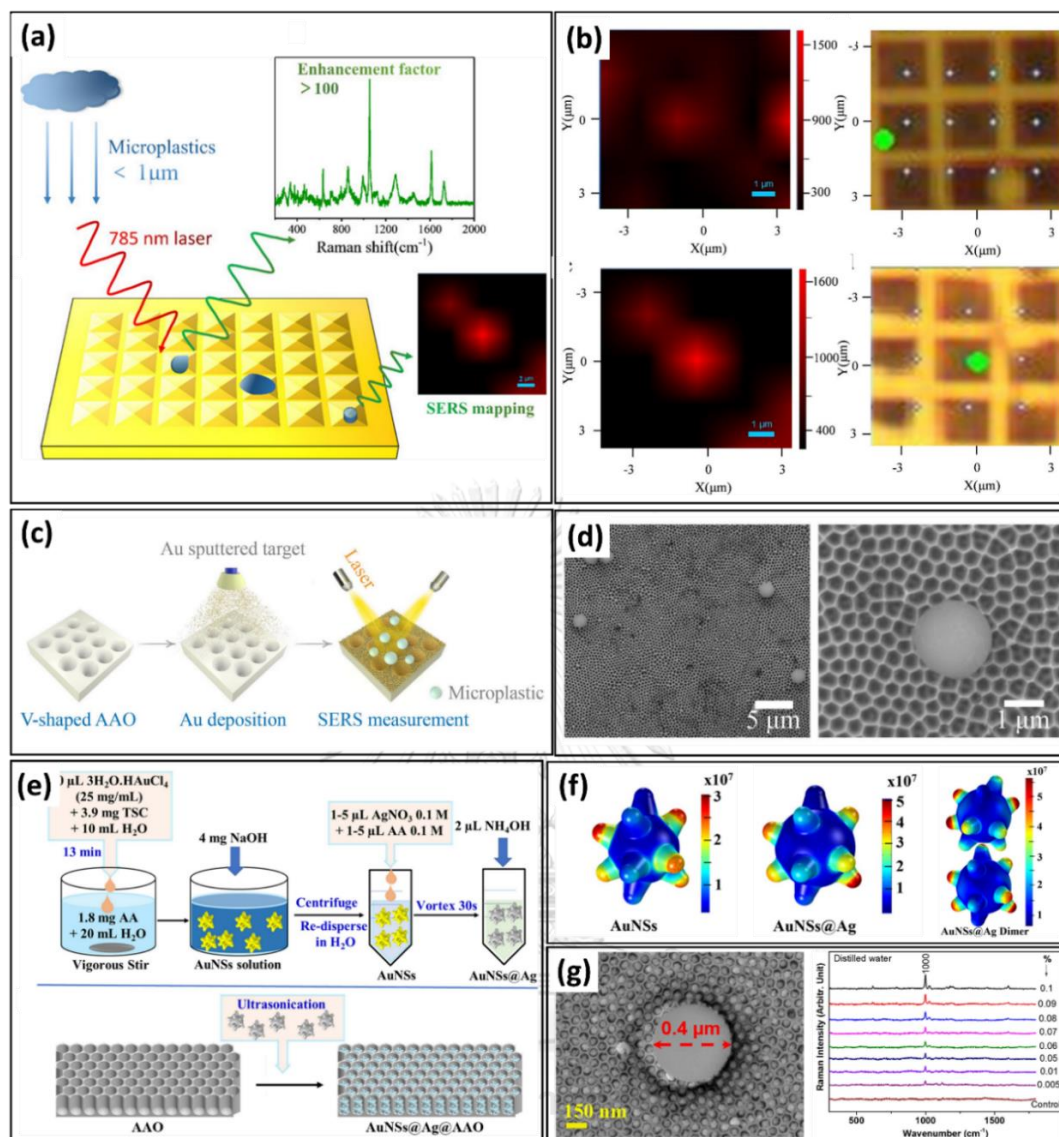


Figure 6. (a) schematic drawing of NPLs detection in the atmospheric environment by Karite substrate utilized mapping technique, and (b) mapping image of NPLs with particle size 360 nm (up) and 500 nm (down) obtained from the mapping area on Karite substrate shown in OM image [56]. (c) schematics drawing of AuNPs@V-shaped AAO substrate fabrication process and (d) SEM image of PSMSs (diameter = 2 μm) on AuNPs@V-shaped AAO substrate in different magnifications [170]. (e) schematic drawing of AuNSs@Ag@AAO substrate preparation and (f) COMSOL simulation of the localized electromagnetic fields of the AuNSs monomer, AuNSs@Ag monomer, and AuNSs@Ag dimer (3D model) and (g) SEM images of 400 nm of PS particles on the SERS substrate with their SERS spectra at different concentrations [58].

In the same way, Li *et al.* [173] proposed a particle in the cavity of an AAO structure covered with MoS₂ and immobilized with AgNPs. By treating and modulating the cascaded optical-field mode within the cavity, the redesigned AAO cavity structure with MoS₂/AgNPs effectively combines both surface hot spots (SHSs) or localized hotspots (LHSs) and volume hot spots (VHSs). In this study, NPLs were detected by immersing the substrate in a suspension of NPLs, allowing the NPLs to insert into the cavities of the substrate, as shown in the SEM image in **Figure 7a**. The results showed that the SERS intensity of PSNSs with a diameter of 100 nm was approximately 1.5 times greater than that of NSs with diameters of 200 and 300 nm, due to variations in the arrangement of LHSs and VHSs within the distinct structure (**Figure 7b**). The presence of more NPL spheres within the cavity amplified the scattering effect, enhancing the combination of LHSs and VHSs with smaller NPLs. Therefore, this approach allowed for better identification and detection of NPLs with particle sizes less than 300 nm in water (**Figure 7c-d**).

In contrast to rigid substrates such as glass and silicon wafers, porous structure-based polymer provides superior flexibility and 3D structure, allowing for the fabrication of high SERS performance-based detection. Yin *et al.* [174] utilized a flexible and porous gold-modified sponge as a SERS substrate for detecting plastic particles in various testing environments without the need for sample pretreatment. In this work, the substrate was fabricated using a layer-by-layer assembly. As illustrated in **Figure 8a**, the sponge was first soaked in a PDDA solution and then exposed to an AuNPs solution, forming a gold-modified bowl-shaped structure on the sponge surface. MPLs suspended in different water samples were filtered and trapped within the sponge structure for analysis. This method enabled the detection of MPLs in seawater, snow, river, and rainwater. However, due to the relatively large pore size of the sponge (average diameter = 39 μm), as shown in **Figure 8b**, NPLs with sizes larger than 1 μm would not be captured and examined using this method. Additionally, this approach required a large volume of samples and employed a high concentration of MPLs (100 $\mu\text{g/mL}$) for detection.

In addition, utilizing regenerated cellulose (RC) film as a support layer may increase NPLs detection performance. According to Jeon *et al.* [61] SERS-active array substrates with RC and plasmonic nanoparticles (Au nanorods (AuNRs) and Ag

nanowires (AgNWs)) were fabricated using a simple vacuum-assisted filtering technique with a silicon mask for rapid NPLs detection (**Figure 8c**). When a plastic solution was drop-casted onto the substrate, PSNSs as small as 84 nm were successfully trapped within the RC film (**Figure 8d**) and detected with high sensitivity. The comparison between AuNRs and AgNWs-based RC substrates showed that AgNWs exhibited stronger SERS activity due to their strong plasmonic effect, resulting in a larger number of active hotspots and a higher enhancement factor (1.8×10^7) compared to AuNRs (5.4×10^6). However, using both metal nanoparticles demonstrated sufficient sensitivity for NPLs detection in water, the concentration required for detection was still relatively high (100 $\mu\text{g/mL}$).

To address the issue of low LOD, Yang *et al.* [68] proposed a hybrid method that combines membrane filtration and SERS for the analysis of trace NPLs in water. They utilized a bi-functional nanowire membrane consisting of self-assembled silver nanowires (AgNWs) to enrich the nanoplastics and enhance their Raman signal for detection. The fabrication of the SERS substrate involved the flow-through method, as depicted in **Figure 8e**. A commercial filter paper with a pore size of 15–20 μm was used as a support, and the AgNWs solution flowed through it to form the AgNWs membrane *via* self-assembly. The NPLs suspension was then passed through the membrane, where the NPLs were trapped on the substrate, enabling SERS measurement with Raman mapping in situ. With this approach, NPLs as small as 50 nm could be trapped by the AgNWs on the substrate (**Figure 8f**). The Raman mapping technique allowed for the detection of NPLs with a diameter of 50 nm at a concentration as low as 0.1 ng/mL (**Figure 8g**), which is comparable to the natural concentration of NPLs found in environmental samples.

According to the study findings, numerous researchers have developed the SERS technique for practical applications. SERS technology has significant benefits in evaluating NPLs and provides a method for detecting NPLs in the actual world. However, the size-dependent effect poses a challenge for detection, as the SERS intensity of NPLs is influenced by their size rather than their concentration. This limitation hinders the construction of standard curves for quantitative analysis of NPLs and limits the linear range for their quantification. For instance, when using the

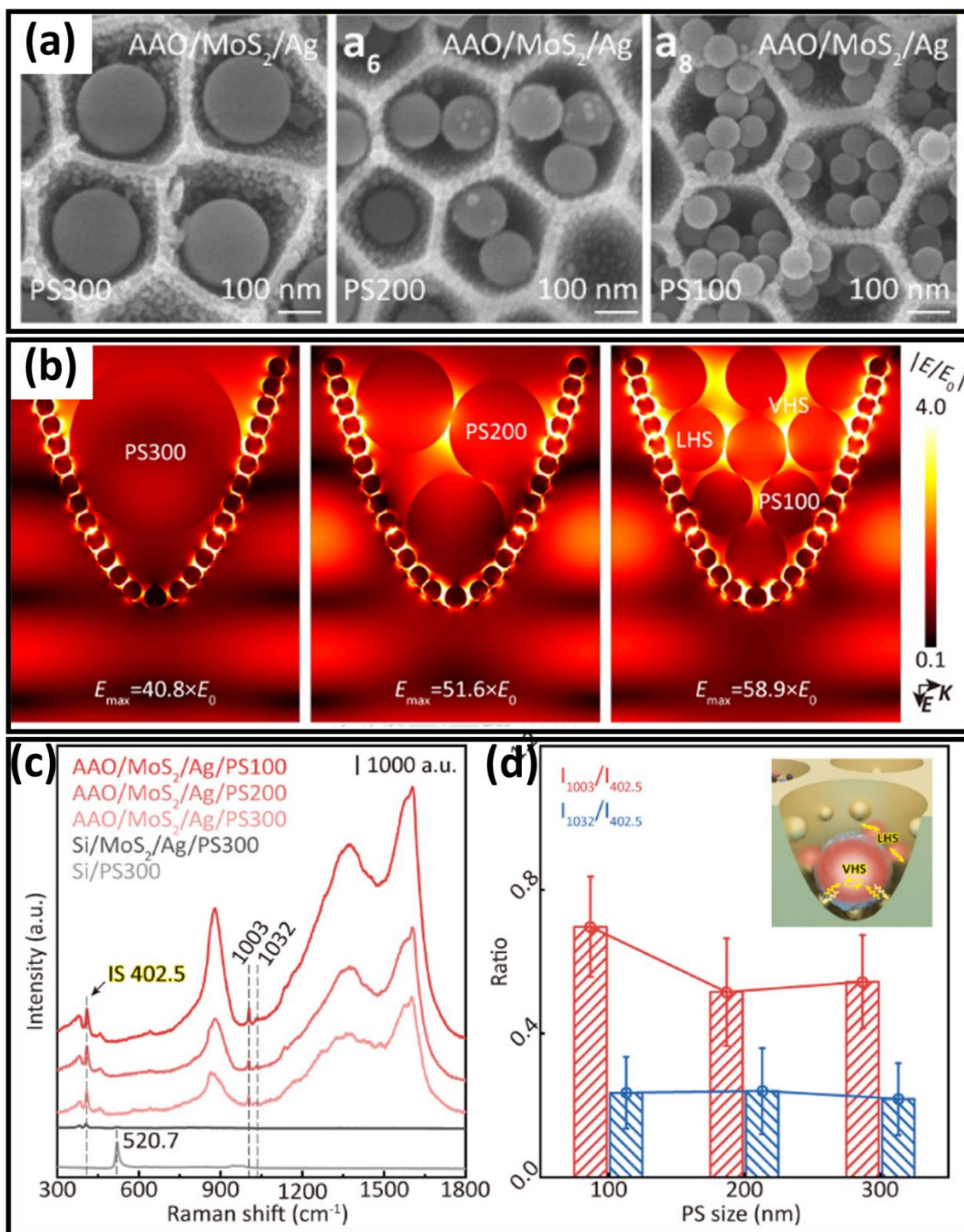


Figure 7. (a) SEM image of Si/MoS₂/Ag substrate with PSNSs with different sizes (*i.e.*, 100, 200, and 300 nm). (b) electric-field distributions in AAO/MoS₂/Ag cavities by employing FDTD simulations. (c) Raman and SERS spectra of AAO/MoS₂/Ag, Si/MoS₂/Ag, and Si substrate with different sizes of PSNSs. (d) comparison of the SERS intensity ratio of NPLs with different sizes [173].

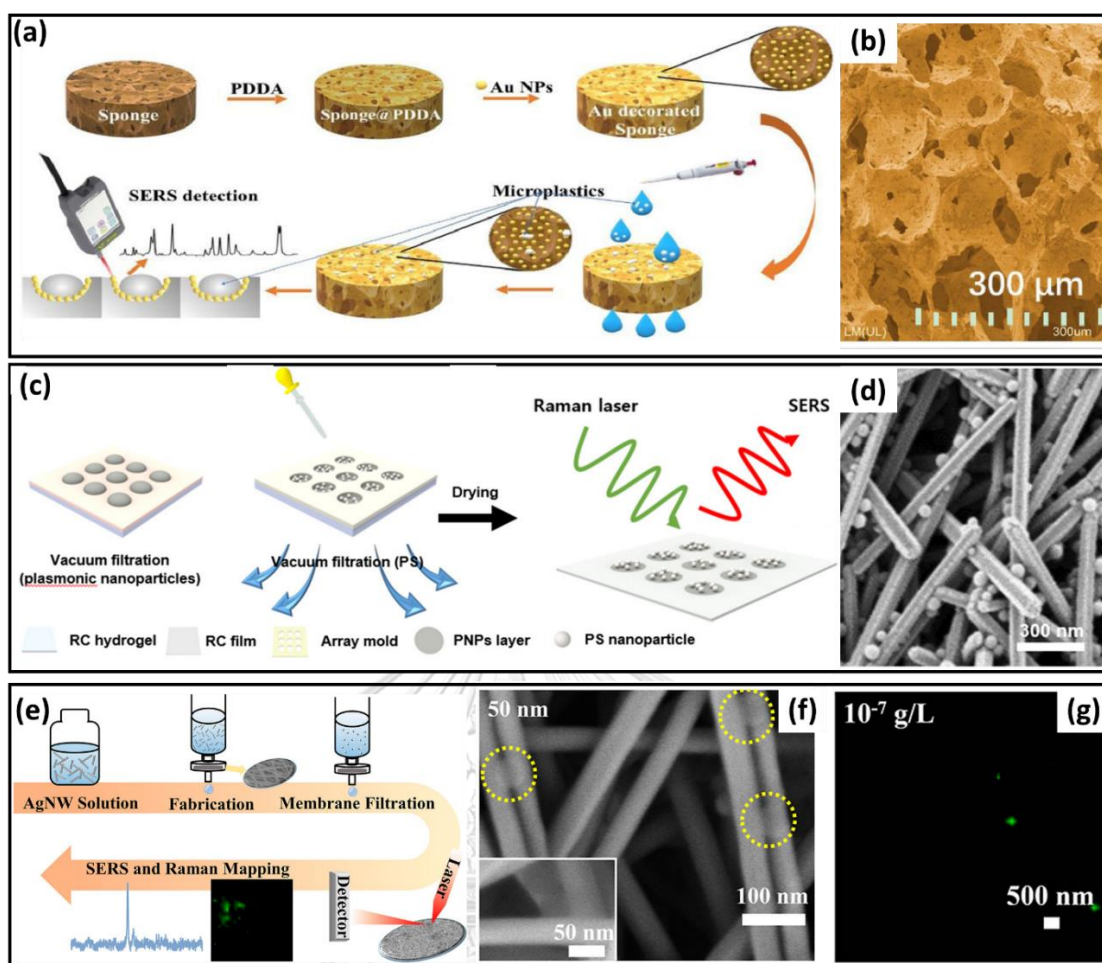
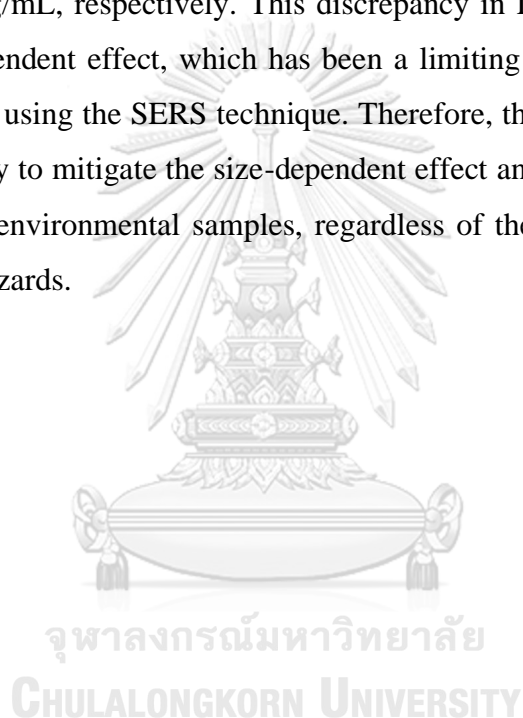


Figure 8. (a) schematic illustration of AuNPs decorated sponge to detect MPLs in water and (b) OM images of sponge substrates [174]. (c) schematic illustration of the fabrication of PNPs/RC films and (d) SEM image of 84 nm PSNs on an AgNWs/RC film [61]. (e) preconcentration and detection of NPLs using membrane filtration and SERS, (f) SEM images of 50 nm standard PSNs retained on the membrane, and (g) Raman mapping images of 50 nm PSNs with concentration of 0.1 ng/mL [68].

Karite substrate, SERS signals from NPLs of different sizes exhibited varying intensities. This is attributed to the variation in enhancement power associated with different NPL sizes. The plasmonic electric-field distribution within the Karite cavity is concentrated in the lower portion, and NPLs with a diameter of 360 nm fit precisely within this region where the plasmonic electric field is strongest, resulting in a more pronounced SERS activity compared to larger NPLs with diameters of 500 nm or larger located in the upper portion of the cavity [56].

Furthermore, suspension-based detection methods also encounter challenges due to the size-dependent effect, as different-sized NPL particles (such as 300 nm and 500 nm) exhibit varying aggregations, leading to fluctuations in SERS activity caused by changes in hot spot distribution [57]. Moreover, even when a linear range is established, the limit of detection (LOD) for plastic particles of different sizes can vary significantly. For instance, in the study by Hu *et al.* [57], the LOD values for detecting PSNSs with diameters of 50 nm, 100 nm, and 200 nm at the same concentration differed. The LOD values were approximately 12.5 $\mu\text{g/mL}$, 6.25 $\mu\text{g/mL}$, and 25 $\mu\text{g/mL}$, respectively. This discrepancy in LOD values directly arises from the size-dependent effect, which has been a limiting factor for the quantitative detection of NPLs using the SERS technique. Therefore, there is an urgent need for a new SERS strategy to mitigate the size-dependent effect and accurately quantify NPL concentrations in environmental samples, regardless of their size, in order to assess their ecological hazards.



CHAPTER III

MATERIALS AND METHODS

3.1 Materials

All chemicals were purchased from different suppliers: PS beads with diameters of 100, 300, 600, and 800 nm, albumin, magnesium chloride (MgCl_2), sulfuric acid (H_2SO_4), and hydrogen peroxide (H_2O_2) were purchased from Sigma-Aldrich. Sodium chloride (NaCl), calcium chloride (CaCl_2), and potassium chloride (KCl) were obtained from Carlo Erba Reagents. Glucose and galactose were purchased from Univar. Fructose, sucrose, arabinose, sodium dodecyl sulfate (SDS), and toluene were purchased from VWR Chemicals, Ajax Chemical, Fluka BioChemica, Kemas, and RCI Labscan, respectively. Ultrapure water ($18.2 \text{ M}\Omega\cdot\text{cm}$ at 25°C) was produced using a Milli-Q gradient system from Massachusetts, United States. Tap water was sourced from the 10th-floor, Faculty of Science, Chulalongkorn University, Bangkok, Thailand. Chaophraya river water was collected from ICONSIAM, Bangkok, Thailand. Mineral water (Purrá) was commercially available by Singha Company Co., Ltd, Thailand.

3.2 Preparation and characterization of SERS substrate

A glass cover slide was used as a support to prepare the SERS substrate. To remove any organic contaminants, the glass slide was first soaked in Piranha solution ($\text{H}_2\text{SO}_4 : \text{H}_2\text{O}_2$, 2:1v/v) overnight. After cleaning process, the glass slide was coated with gold particles using a gold sputtering equipment (Quorum, Q150R S, Leica, EM CPD300, United Kingdom). The sputtering process involved applying a voltage of 15 mA and maintaining a distance of approximately 7 cm between the sample surface and the probe. The sputtering time varied from 30, 60, 90, 120, 150, to 180 s, which was the maximum sputtering time/round of the instrument. AFM instrument (Seiko Instruments, SPI3800N / SPA400, Japan) was also used to characterized surface roughness and thickness of SERS substrates in this study.

3.3 SERS measurement

Five hundred μL of PSNSs suspension were dried in glass vial under vacuum conditions to remove an water medium. Next, 50 μL of toluene was added to dissolve the PS particles, resulting in a homogeneous solution. This dissolution process took 1 minute, and the NPLs (presumably referring to the PSNSs) were completely dissolved in toluene, as observed in **Figure S1**). Then, a 3 μL droplet of the PS solution was placed on the previously prepared SERS substrate surface and allowed to dry, forming a thin PS film. SERS spectra of the PS films were recorded using a Raman microscope (Thermo Scientific DXR Raman microscope, USA), equipped with a 532-nm excitation laser and a 100X objective lens. For each sample, SERS spectra were collected from 3 different droplets, and within each droplet, 5 spectra were acquired from different regions. To prevent damage of the PS film as an analyte due to heating, the laser power was optimized to 5 mW for the measurements. The exposure time and accumulation number were both set to 2 s, and the laser spot size was approximately 0.5 μm .

3.4 Preparation of real-world media samples

In this study, various types of real-world media such as tap water, mineral water, and river water were chosen. Initially, 10 wt.% of PSNSs with sizes of 100, 300, 600, and 800 nm were combined in equal ratios (1:1:1:1). Instead of using Milli-Q water, each step of the dilution process involved the addition of the each real-world media separately. The resulting mixture was then used to create NPLs at different concentrations ranging from 10, 20, 30, 40, 50, 60, to 70 $\mu\text{g}/\text{mL}$, with a total volume of up to 500 μL .

CHAPTER IV

RESULTS AND DISCUSSION

4.1. Characterization of SERS substrate

To optimize the enhancement factor of the SERS substrate, the sputtering time for gold coating was varied at 30, 60, 90, 120, 150, and 180 s. The surface roughness (**Figure 9a**) and thickness (**Figure 9b**) of the gold coating on the substrate were examined using AFM micrographs. The results suggest that the sputtering time has an influence on the roughness and thickness of gold on the glass slide surface, which could directly affect the SERS intensity of NPLs. However, as shown in **Figure 9c**, the surface roughness of the SERS substrates did not significantly differ when the sputtering time was between 60 to 180 s, indicating that a sputtering time exceeding 60 s can achieve uniformity of the SERS substrates. It also implies that the surface roughness of the SERS substrate at any sputtering time might not have a significant impact on the SERS enhancement. The SEM technique was also employed to examine the surface morphology of the SERS substrate, and the results showed similar characteristics when the sputtering time exceeded 60 s (**Figure S2**). Conversely, the sputtering time did affect the linear increase in gold film thickness, with measurements of 11.3, 15.5, 19.6, 23.8, 28.1, and 32.1 nm, as shown in **Figure 9d**. The increase in film thickness is attributed to the deposition of more gold particles on the SERS substrates over time. This deposition process enables the SERS substrates to amplify the Raman intensity of NPLs analytes. **Figure 9e**, demonstrates that the SERS intensity of PS (specifically the intensity at 1005 cm^{-1} , I_{1005} , corresponding to the ring breathing mode of PS) increases with an increase in film thickness. The SERS spectra of PS on the SERS substrate at different sputtering times are provided in **Figure S3**. Notably, the substrate with a gold thickness of approximately 32.1 nm exhibited the highest SERS intensity for the NPLs, with an enhancement factor reaching 4.2×10^8 (detailed calculation can be found in Supplementary Material, **Figure S4**). This can be attributed to the dense electromagnetic field at the surface of the SERS substrate. Moreover, the SERS performance uniformity of the SERS substrate at a sputtering time of 180 seconds is not significantly different from the others. This is supported by the standard deviation

values of SERS intensities from NPLs at different sputtering times, which were 9.82, 10.67, 7.58, 10.46, 7.04, and 10.39 for the sputtering times of 30, 60, 90, 120, 150, and 180 s, respectively. Consequently, the SERS substrate with a sputtering time of approximately 180 s (exhibiting the highest SERS activity) was chosen for further measurements of NPLs.

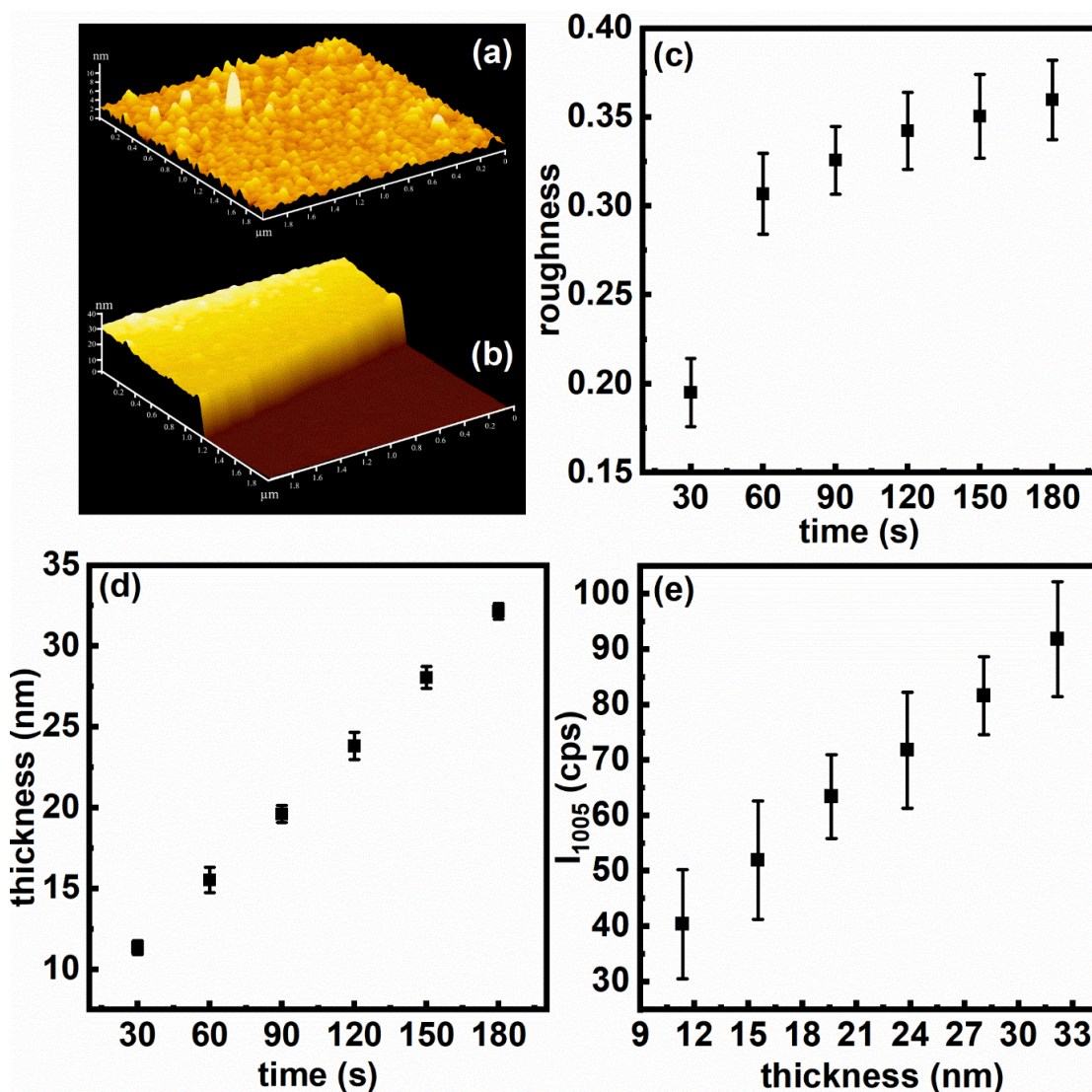


Figure 9. AFM micrographs of the SERS substrate show (a) surface roughness and (b) gold film thickness of the SERS substrate with a 180-second sputtering time. Plots of (c) roughness versus sputtering time, (d) gold film thickness versus sputtering time, and (e) I_{1005} versus gold film thickness. PS latex beads with a diameter of 600 nm were prepared at the concentration of 10 $\mu\text{g/mL}$, for these SERS measurements.

4.2. Standard calibration curve for PSNPs with various particle sizes

The SERS spectra were collected at the edge of the dried droplets, where the PS molecules formed a film on the surface of the SERS substrate. These spectra were used to construct standard calibration curves for quantitatively measuring PS particles in aqueous media. An optical microscope (OM) image in **Figure 10a** shows the PS film on the SERS substrate at the edge of the dried droplet. Data collection was performed along the edge of the film as indicated in **Figure 10a(i-v)**. Due to the coffee-ring effect, the edge appears thicker compared to the middle region. This effect is caused by solvent evaporation in PS solutions, leading to capillary flow and the migration of PS molecules from the center to the rim of the droplet. Consequently, after drying, PS molecules are concentrated along the edge of the droplet. The SERS spectra acquired from different locations along the border are shown in **Figure 10b(i-v)**. It can be observed that the spectra from these locations exhibit similar patterns, especially in the range of 600-1600 cm^{-1} , which are the unique fingerprint spectra of PS polymer (see **Figure S5**). These SERS spectra resemble the spectrum of the original PSNPs, indicating that the toluene solvent can dissolve PSNPs without altering the chemical properties of PS molecules. The prominent characteristic peaks of PS can be observed in the SERS spectra, including peaks at 623, 1005, 1030, 1201, and 1607 cm^{-1} , corresponding to the ring deformation mode, ring breathing mode, C–H in-plane deformation mode, C–C stretching mode, and ring skeletal stretching mode, respectively. [176, 177]. Furthermore, the SERS spectra of PS appear clean and clear, without interference from the toluene solvent spectrum, as it evaporates rapidly, leaving behind the PS molecules to be detected at the dried droplet edge. **Table S1** provides a comprehensive overview of the peak assignments based on the peak positions of PS. Among these peaks, the peak at 1005 cm^{-1} has been commonly used in previous investigations [49, 57, 178] to confirm the presence of PS polymer due to its strong Raman signal compared to other peaks. [56]. Therefore, in this study, a calibration curve was developed using the unique peak at 1005 cm^{-1} for the quantitative determination of NPLs in aqueous media.

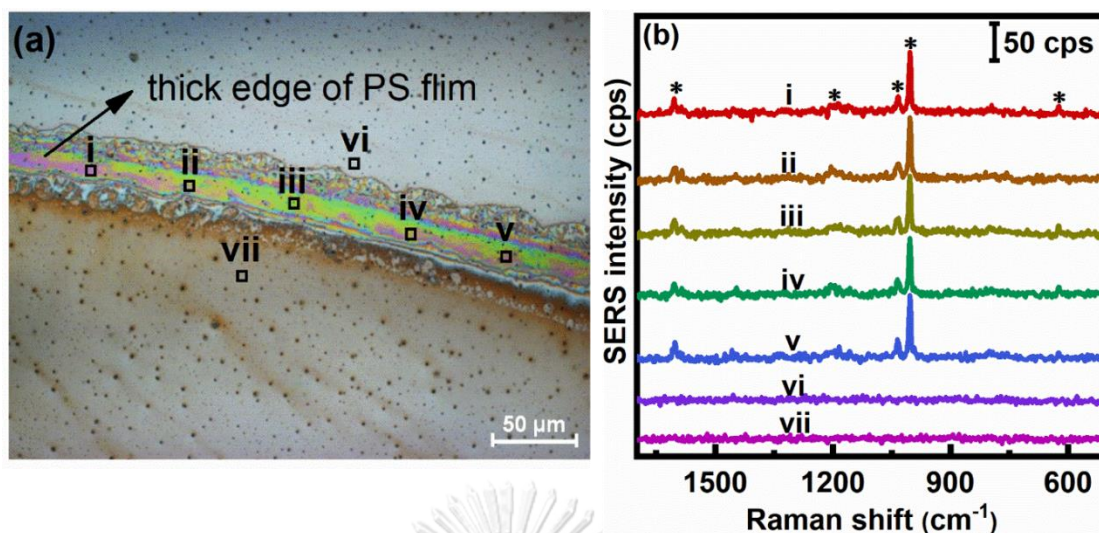


Figure 10. (a) OM image and (b) SERS spectra of PS film (i–v) at the edge of, (vi) inside, and (vii) outside the dried droplet. The experiment was carried out using PSNSs with a particle size of 600 nm at a concentration of 10 $\mu\text{g/mL}$.

However, in **Figure 10b**, the spectrum of PS could not be detected at positions “vi” and “vii”, which correspond to locations inside and outside the dried droplet, as indicated by the OM image in **Figure 10a**. The results indicate that the evaporation of the PS droplet leads to the accumulation of PS molecules at the droplet boundary, a phenomenon known as the coffee-ring effect. This effect is advantageous for the preconcentration of plastics, especially at extremely low concentrations. [179-181]. Additionally, using this phenomenon, the SERS spectra of plastics become prominent even at a concentration of 10 $\mu\text{g/mL}$, which has not been utilized for the quantification of NPLs in previous studies [57, 58, 61, 69, 174]. Consequently, this SERS approach enables the detection of NPLs even at low concentrations. **Figure 11a** displays the SERS spectra of PS in the 990–1020 cm^{-1} region for various PS concentrations (*i.e.*, 10, 20, 30, 40, 50, 60, and 70 $\mu\text{g/mL}$) using PSNSs with a particle size of 600 nm. Typically, the intensity of I_{1005} , which corresponds to PS, is expected to increase as the concentration of NPLs increases. However, it was observed that the signal of PS polymer only changed within the concentration range of 10 to 40 $\mu\text{g/mL}$. The SERS intensity of PS did not show significant changes at concentrations above 40 $\mu\text{g/mL}$. This can be attributed to the thickness of the PS film, which may exceed the enhancement area provided by the gold layer, as illustrated in **Figure 12**. As a result, the enhanced electric field from the SERS substrate cannot effectively reach

the top part of the PS film. It should be noted that molecules can be normally enhanced when they are in close proximity to the metal surface with a distance of less than 10 nm, as supported by previous studies [163, 182]. This is the reason why the SERS intensity did not further increase but remained constant at approximately 215 cps when the PS concentration exceeded 40 $\mu\text{g/mL}$, as shown in **Figure 11b**.

Additionally, the same experimental procedure was conducted using PSNSs with other particle sizes (*i.e.*, 100, 300, and 800 nm), and a similar trend was observed (**Figure S6**) compared to the PSNSs with a particle size of 600 nm shown in **Figure 11a**. This finding indicates that our proposed preparation procedure effectively eliminates the size-dependent effect caused by different sizes of PSNSs. Consequently, this result provided motivation for testing PSNSs with mixed particle sizes in the subsequent section.

To assess the influence of PS particle size on the construction of standard calibration curves, PS particles with sizes of 100, 300, 600, and 800 nm were utilized. The limits of detection (LODs) were determined based on the standard deviation of the response (σ) and the slope of the calibration curve (S), using the equation, $LOD = \frac{3.3\sigma}{S}$. Based on **Figure 4b**, the SERS intensity of NPLs with different sizes at the same concentrations exhibited no significant differences. This finding demonstrates the ability of the method to overcome the size-dependent effect of NPLs. Moreover, this method can be employed for quantitative analysis of PSNSs within the concentration range of 10–40 $\mu\text{g/mL}$ with LODs of 0.26, 0.17, 0.10, and 0.10 $\mu\text{g/mL}$ for the PSNSs with particle sizes of 100, 300, 600, and 800 nm, respectively.

In comparison to mass spectroscopic methods like pry-GC-MS, our SERS quantitative detection method involves several steps due to the absence of sample preprocessing techniques in pry-GC-MS. Pry-GC-MS, on the other hand, is a time-consuming approach with a complex operational process. It requires manual placement of particles into a pyrolysis tube and can analyze only one MPLs per cycle, which is insufficient for large sample volumes. In contrast, the SERS technique offers a more rapid and straightforward approach and has the potential to be utilized for on-site quantitative analysis.

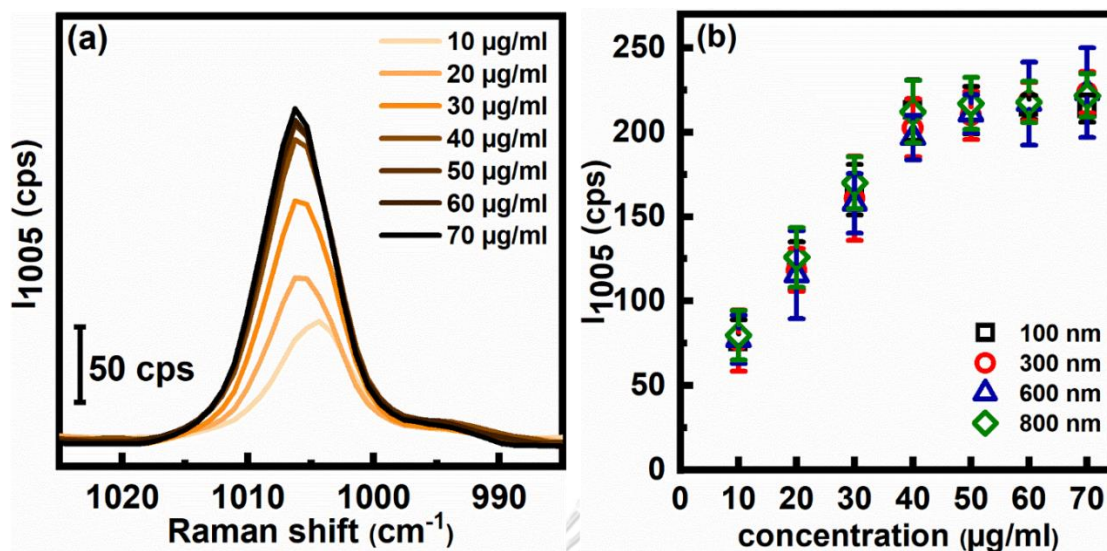


Figure 11. (a) SERS spectra of PS in the region of 990–1020 cm^{-1} at different PS concentrations, and (b) standard calibration curves of PS with particle sizes of 100, 300, 600, and 800 nm.

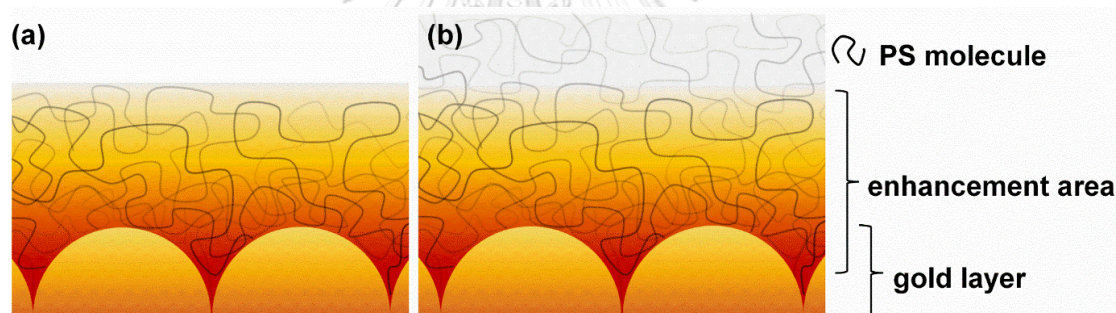


Figure 12. Schematic drawing for the SERS enhancement area of the substrate. PS films are deposited (a) in and (b) over the enhancement area of the SERS substrate.

4.3 Effect of interferences

In this section, we added individual interferences to DI water as part of our evaluation process to determine the selectivity of our protocol in detecting NPLs. The concentration of NPLs remained constant at 10 $\mu\text{g/mL}$ for each particle size, while each interference substance was prepared at a concentration of 0.1 wt.%. We measured the SERS spectra of each individual interference, as depicted in **Figure S7**. It can be seen that the Raman spectra of salts such as NaCl, KCl, MgCl_2 , and CaCl_2 could not be observed since they do not exhibit Raman activity. However, sugars (*i.e.*, sucrose, glucose, fructose, arabinose, and galactose) and a detergent (SDS) produced

strong SERS signals in the 3200–2800 and 1600–300 cm^{-1} regions. Additionally, albumin protein showed a distinct Raman fingerprint, particularly at the peak of 1005 cm^{-1} , which coincides with the peak of the PS used for evaluation in our study. Notably, the presence of albumin has the potential to influence the detection, identification, and quantification processes of NPLs.

Fortunately, the suspension of NPLs along with each interference was dried and then redissolved using an organic solvent before being applied to the SERS substrate for data acquisition. In this particular step, toluene, an organic solvent with non-polar properties, was utilized as a suitable medium to completely dissolve the PS beads, which are non-polar polymers. This choice was based on the principle that "like dissolves like." As a result, the various interferences (which are polar substances) that typically dissolve in water (a polar solvent) were effectively separated during this process. Consequently, the concentration of interferences in the PS solution was significantly reduced before it was dropped and dried onto the SERS substrate. Additionally, it was observed that during the drying process on the substrate, a tiny amount of interference was dried and separated from the edge of the PS film, as clearly demonstrated in **Figure 13a**. The SERS signals of the PS film in the presence of interference were collected from the square area on edge labeled from "i"–"v". This area also contained the dried droplet labeled from "vi"–"ix",

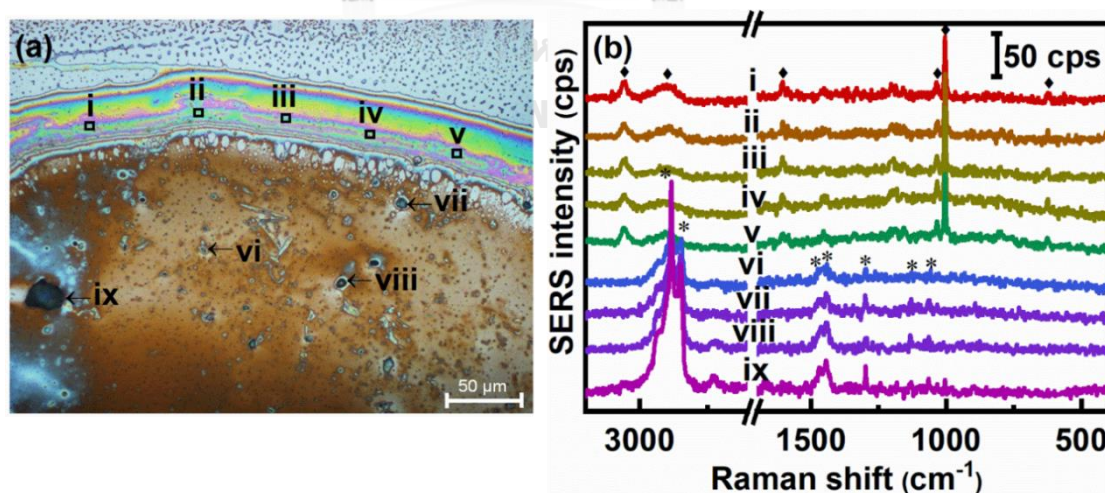


Figure 13. (a) OM image and (b) SERS spectra of PS film prepared from 600-nm PSNSs suspension with SDS interference using our proposed method at different positions.

where the presence of both PS and interference was detected. The SERS spectra shown in **Figure 13b** confirm the existence of PS and interference in the region labeled “i”–“ix” in **Figure 13a**.

The acquisition area between “i”–“v” exhibited a strong and clear PS spectrum without any interference signal (such as SDS) noticeable in the spectrum. On the other hand, the SDS spectra obtained within the droplet region labeled from “vi”–“ix” showed a distinct peak at around 2880 cm^{-1} without the presence of the PS signal. This demonstrates the high effectiveness of our preparation procedure in detecting PSNSs, which exhibit a strong signal even at a low concentration ($10\text{ }\mu\text{g/mL}$). **Figure 13(a–b)**, consistently display the SERS spectrum of PS, as the interference and PS were deposited separately onto the SERS substrate in distinct and separate areas. Consequently, these PS beads with nanometer diameters can be successfully detected, identified, and quantified even in the presence of various interferences.

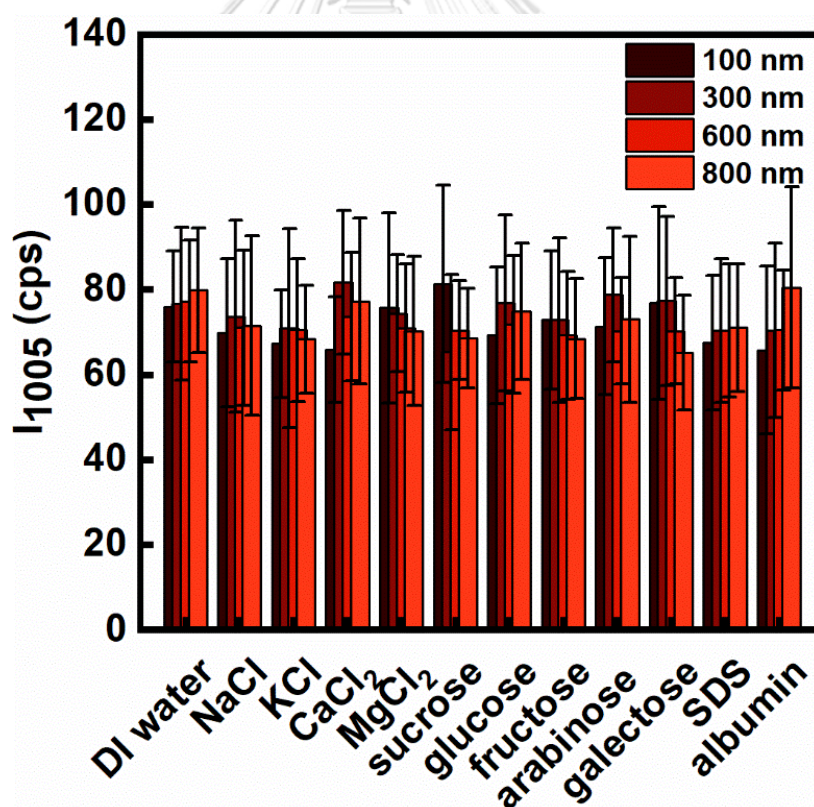


Figure 14. I_{1005} of PS films prepared from PSNSs suspensions with various interferences, *i.e.*, NaCl, KCl, MgCl₂, CaCl₂, sucrose, glucose, fructose, arabinose, galactose, SDS, and albumin.

Figure 14 illustrates the SERS intensity of NPLs (I_{1005}) with different particle sizes (*i.e.*, 100, 300, 600, and 800 nm) in the presence of various interferences at a PS concentration of 10 $\mu\text{g/mL}$. The results indicate that there is no significant variation in SERS intensity among NPLs with different sizes in present of salts (*i.e.*, NaCl, KCl, MgCl_2 , and CaCl_2), sugars (*i.e.*, sucrose, glucose, fructose, arabinose, and galactose), detergent (SDS), and protein (albumin). This study provides confirmation that our preparation protocol is effective for analyzing PSNSs of different sizes in the presence of diverse interferences.

4.4 Detection of PSNPs in real-world media

In this section, a mixture of PSNSs with diameters of 100, 300, 600, and 800 nm was prepared using a mass ratio of 1:1:1:1. The PS concentration in the mixture was varied, ranging from 10, 20, 30, 40, 50, 60, to 70 $\mu\text{g/mL}$. The purpose was to create a standard calibration curve that can be used for quantitatively analyzing the PS concentration in various types of real-world media, including DI water (as a control medium), tap water, mineral water, and river water.

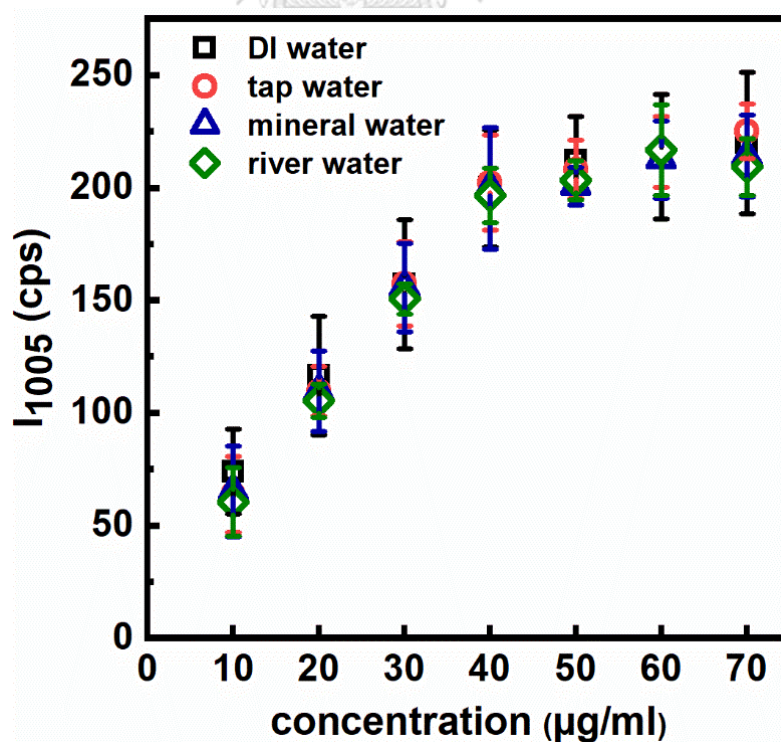


Figure 15. Plots of I_{1005} against the PS concentration in real-world media, including DI water (control medium), tap water, mineral water, and river water.

Table 2. The LODs of previously published SERS approaches compared with our study.

SERS substrate	type of NPLs	LOD	media	ref.
Au nanopore fabricated at the tip of a glass nanopipette	PS (20 nm) and PMMA (10 nm)	500 µg/mL	water	(Nie <i>et al.</i> , 2019)
AgNPs	PS (100 and 500 nm), PE and PP (10 µm)	40 µg/mL	pure water and seawater	(Lv <i>et al.</i> , 2020)
Klarite substrates	PS and PMMA	26 µg/mL	environmental sample (airborne particles)	(Xu <i>et al.</i> , 2020)
Ag-coated-Au nanostar	PS (400nm, 80nm, 2.3 µm and 4.8 µm)	50 µg/mL	pure water, seawater, and river water	(Lê <i>et al.</i> , 2021)
AuNPs	PS (161nm and 33 nm) and PET (62 nm)	10 µg/mL	milliQ water	(Caldwell <i>et al.</i> , 2021)
AuNPs-decorage sponge	PET, PE, PVC, PP, and PS (80–150 µm)	1 µg/mL	seawater, rainwater, river water, snow water, and tap water	(Yin <i>et al.</i> , 2021)
AgNWs arrays on RC films	PS (630 nm and 84 µm)	100 µg/mL	water	(Jeon <i>et al.</i> , 2021)
Si-O ₂ self-assembly sputtered with gold film	PS (200 nm)	5 µg/mL	bottled water, tap water, and river water	(Chang <i>et al.</i> , 2022)
AgNPs	PS (50, 100, 200, and 500 nm)	6.25 µg/mL	lake water	(Hu <i>et al.</i> , 2022)
AuNP-doped filter paper	PET (20 µm)	100 µg/mL	pure water	(Xu <i>et al.</i> , 2022)
Silver Nanowire Membranes	PS (100, 300, 500, and 1000 nm)	0.1 ng/mL	water	(Yang <i>et al.</i> , 2022)
Au-sputtered glass slide cover	PS (100, 300, 600, and 800 nm)	0.1 µg/mL	river water, mineral water, and tap water	This work

The plots of I_{1005} against PS concentration in real-world media depicted in **Figure 15**. It is evident that the standard calibration curves for the mixed PSNSs, particularly in DI water, exhibit a similar trend to the previous results shown in **Figure 11a**. This similarity is attributed to our preparation method, which effectively eliminates the influence of plastic particle sizes by dissolving them in an organic solvent to create a homogeneous solution before casting them onto the SERS substrate and measuring the SERS spectra. As a result, the SERS intensity of NPLs is dependent on the concentration rather than the size of the particles. In other words, NPLs of various sizes exhibit the same intensity at the same concentration. This preparation method enabled us to accurately quantify the PS concentration across a range of nanoscale particle sizes. The LODs for PS in these real-world media were found to be 0.48, 0.53, 0.38, and 0.32 µg/mL for DI water, tap water, mineral water, and

river water, respectively. Furthermore, the LOD for NPLs detection achieved in this study demonstrates excellent sensitivity compared to several previous reports utilizing SERS methodology, as summarized in **Table 2**. The consistent LOD values across different real-world media suggest that the media itself does not significantly affect the measurement of PS nanoparticles using our proposed method.



CHAPTER V

CONCLUSIONS

This study presents the development of a SERS approach for the analysis of PSNSs with particle sizes ranging from 100, 300, 600, and 800 nm, which fall below the detection limit of traditional Raman spectroscopy ($>1 \mu\text{m}$). By leveraging the “coffee ring effect” and employing a specific sample preparation technique, SERS measurements were enabled, allowing for the detection of NPLs at extremely low concentrations across various particle sizes. The limit of detection (LOD) achieved for PSNSs detection was $0.10 \mu\text{g/mL}$, with a quantitative range of analysis from 10 to $40 \mu\text{g/mL}$. Importantly, the SERS measurement method proved robust even in the presence of interferences such as NaCl, KCl, MgCl_2 , CaCl_2 , sucrose, glucose, fructose, arabinose, galactose, SDS, and albumin. Moreover, the proposed protocol was successfully applied to determine the concentration of PSNSs dispersed in real-world media, including tap water, mineral water, and river water. The results demonstrate that the developed techniques are simple, cost-effective, and highly suitable for practical applications. The SERS technique holds great promise as a reliable and efficient method for detecting and quantifying NPLs in diverse media, making it particularly well-suited for environmental monitoring purposes.

APPENDIX

SUPPLEMENTARY INFORMATION



Figure S1. Light scattering of (left) the suspension of PSNSs in water and (right) the solution of PSNSs in toluene. NPLs particles with a particle size of approximately 800 nm were employed. The concentration of NPLs in toluene solvent (700 $\mu\text{g/mL}$) was 10 times higher than that of NPLs in water media (70 $\mu\text{g/mL}$).

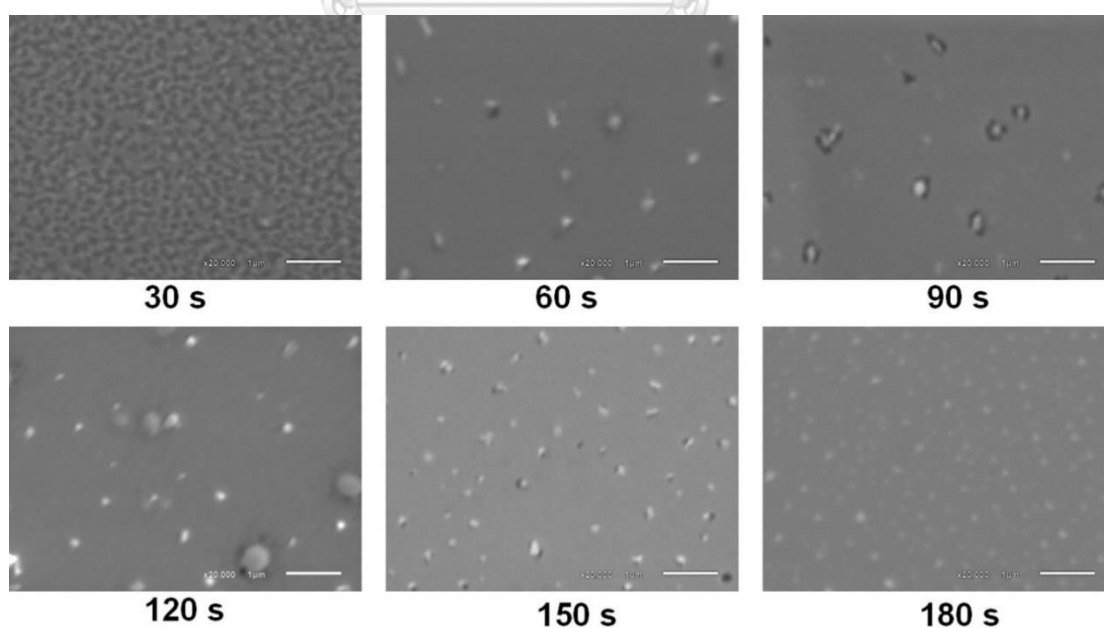


Figure S2. SEM image of SERS substrate surfaces at different sputtering times at 20,000x magnification.

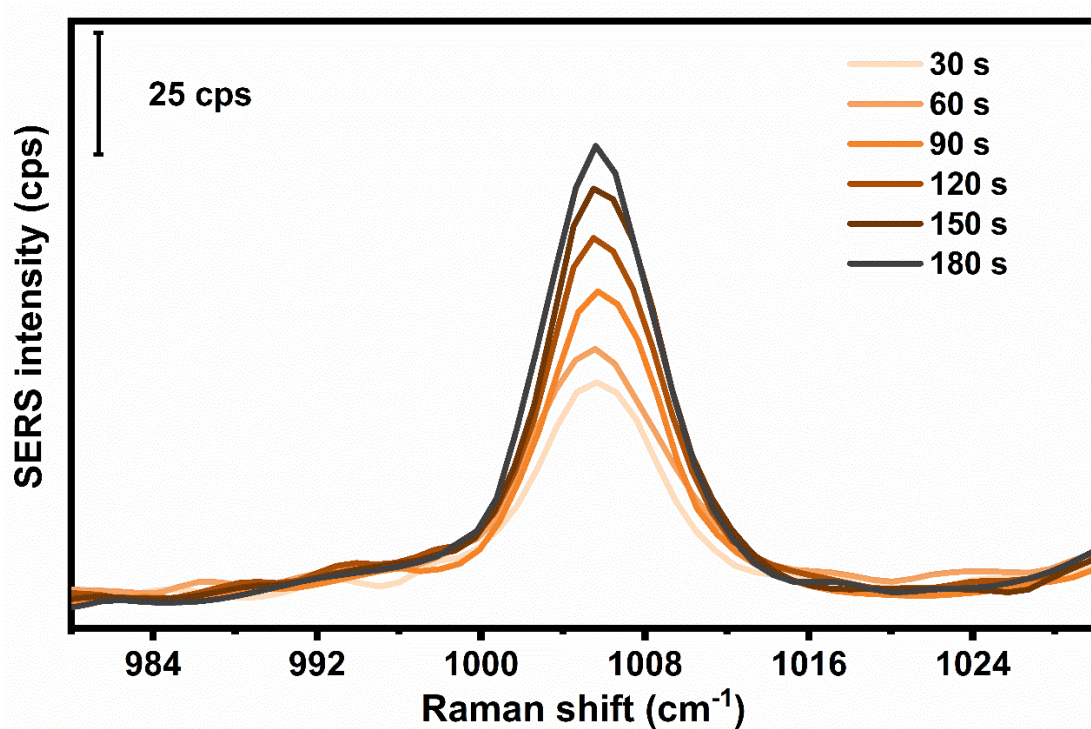


Figure S3. The average SERS spectra of PSNSs on a SERS substrate at different sputtering times (30–180 s).

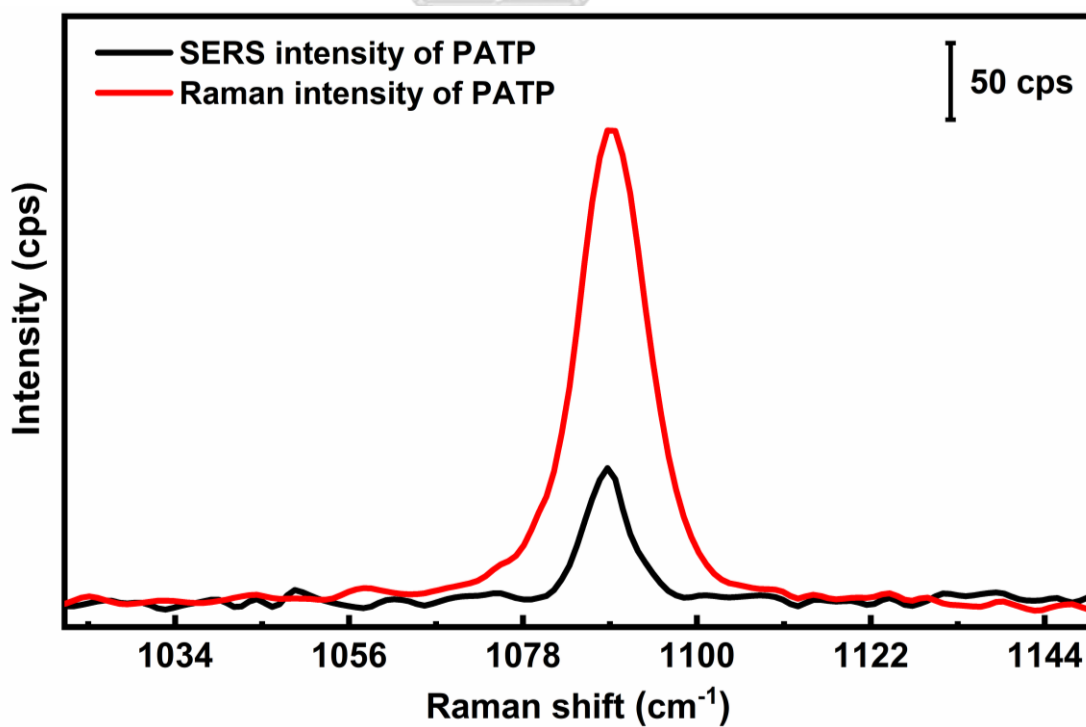


Figure S4. SERS spectrum of PATP on the SERS substrate and normal Raman spectrum of PATP on a glass cover slide at the peak of $\sim 1088 \text{ cm}^{-1}$.

To calculate the enhancement factor (EF) of the substrate, the SERS substrate was soaked in an ethanolic solution of 1.0×10^{-2} M *para*-aminothiophenol (PATP) for 1 hr, and then rinsed with ethanol to remove excess PATP. The substrate was left at room temperature until completely dried before measuring the SERS spectrum (100x objective lens and 2 mW of laser power). To measure the normal Raman of PATP, 1 μ L PATP (0.10 M) was dropped and dried on the glass cover slide before measuring Raman intensity.

The enhancement factor (EF) of a SERS substrate can be calculated as $EF = (I_{SERS}/I_{Raman}) \times (N_{Raman}/N_{SERS})$ where I_{SERS} represents the SERS intensity of the characteristic peak for the analytes adsorbed on the SERS substrate, I_{Raman} represents the normal Raman intensity of the same peak from the analytes on the glass cover slide, and N_{SERS} and N_{Raman} are the number of analytes in the illumination area on the substrate and glass cover slide, respectively.

As shown in **Figure S4**, I_{SERS} and I_{Raman} can be measured at the characteristic peak of PATP (1088 cm^{-1}), which are equal to **85** and **304** cps, respectively.

By assuming that PATP is absorbed as a monolayer on the SERS substrate surface, N_{SERS} can be calculated as $N_{SERS} = A/\sigma$ where A is the laser illumination area (diameter $\sim 0.6 \mu\text{m}$), and σ is adsorbed area of the single PATP molecule, which is 0.2 nm^2 (Zrimsek et al., 2017). Thus, N_{SERS} equals to 1.4×10^6 molecules.

The N_{Raman} can be calculated as $N_{Raman} = A \times \rho$ where A is the laser illumination area (diameter $\sim 0.6 \mu\text{m}$), and ρ is the number of PATP molecules/area of the dried droplet on the glass cover slide ($7.5 \times 10^9 \text{ molecules/nm}^2$). Hence, N_{Raman} equals to 2.1×10^{15} molecules.

Therefore, the EF is approximately calculated as 4.2×10^8 .

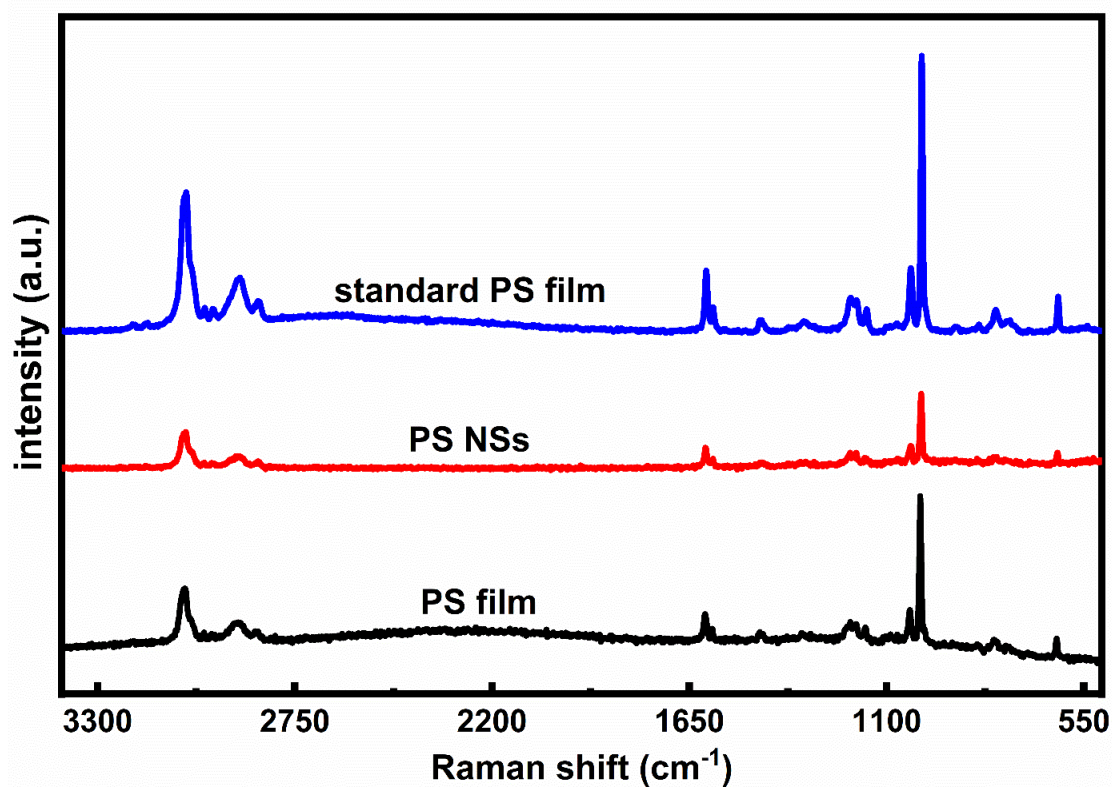


Figure S5. Normal Raman spectrum of standard PS film, normal Raman of PSNSs, and SERS spectrum of PS film. The Raman spectrum of PSNSs was measured at the aggregate of a dry droplet of 1,000 $\mu\text{g/mL}$ PS suspension (800 nm) on the glass cover slide, while the SERS spectrum of PS molecules was detected at the dry droplet edge of PS film (70 $\mu\text{g/mL}$) on top of the SERS substrate.

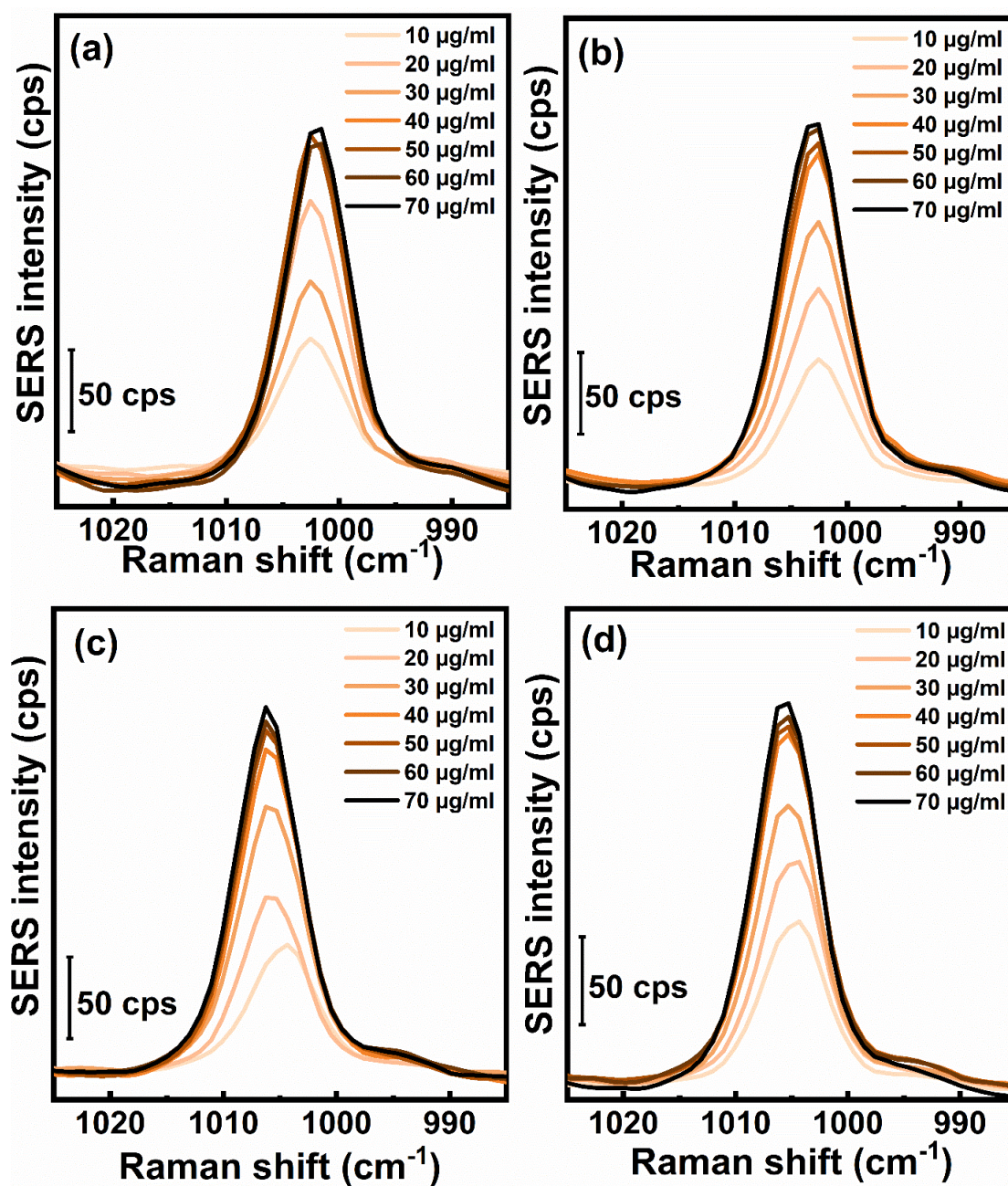


Figure S6. SERS spectra in the region of 990–1020 cm^{-1} of PS films prepared from PSNs with different particle sizes, including (a) 100, (b) 300, (c) 600, and (d) 800 nm. PS concentrations were varied between 10–70 $\mu\text{g/mL}$ for each particle size.

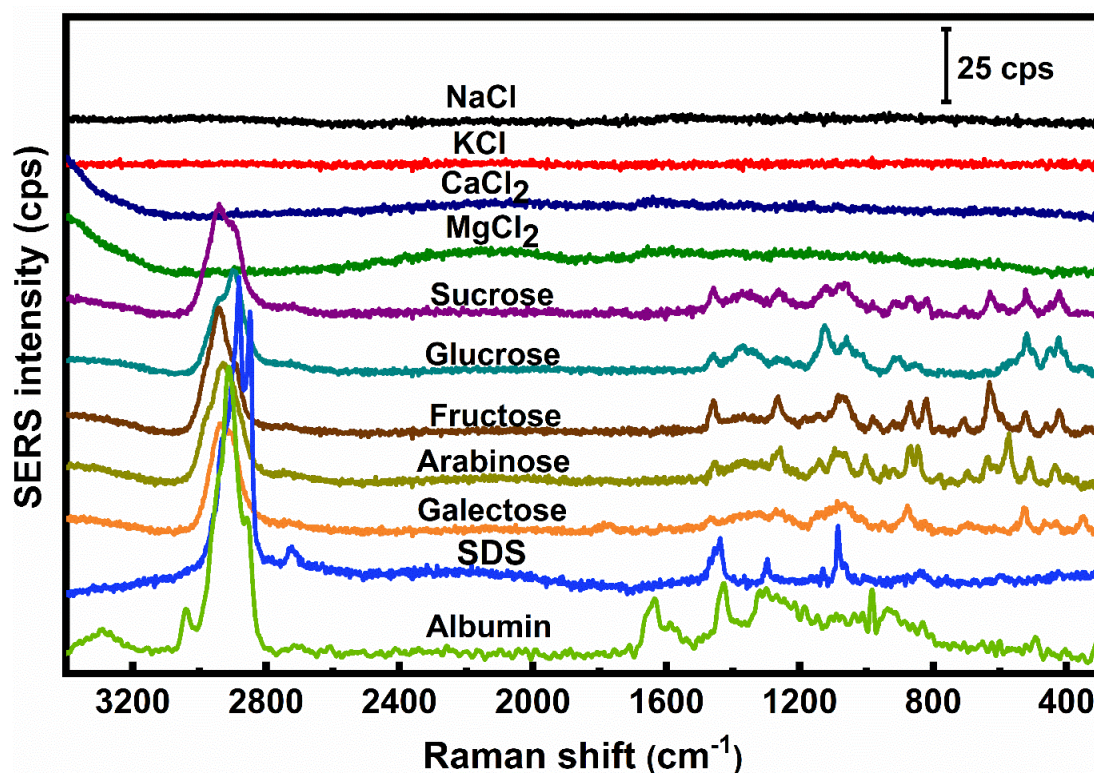


Figure S7. SERS spectra of individual interferences at a concentration of 0.1 wt.%.

Table S1. Peak assignments of a PS film according to peak positions.

peak position (cm ⁻¹)	assignment
623	ring deformation mode
800	C-H out-of-plane deformation mode
1005	ring breathing mode
1030	C-H in-plane deformation mode
1157	C-C stretching mode
1201	C ₆ H ₅ -C vibration mode
1336	C-H deformation mode
1451	CH ₂ deformation mode
1587	C=C stretching mode
1607	ring skeletal stretching mode
2907	anti-symmetric CH ₂ stretching mode
3057	aromatic C-H stretching mode

REFERENCES

- [1] R. Wei, T. Tiso, J. Bertling, K. O'Connor, L. M. Blank, and U. T. Bornscheuer, "Possibilities and limitations of biotechnological plastic degradation and recycling," *Nature Catalysis*, vol. 3, no. 11, pp. 867-871, 2020.
- [2] M. Jefferson, "Whither Plastics?—Petrochemicals, plastics and sustainability in a garbage-riddled world," *Energy Research & Social Science*, vol. 56, p. 101229, 2019.
- [3] I. Tiseo, "Global plastic production 1950–2020," *Statista*, vol. 20, 2021.
- [4] J. N. Hahladakis, C. A. Velis, R. Weber, E. Iacovidou, and P. Purnell, "An overview of chemical additives present in plastics: Migration, release, fate and environmental impact during their use, disposal and recycling," *Journal of hazardous materials*, vol. 344, pp. 179-199, 2018.
- [5] O. S. Alimi, J. Farner Budarz, L. M. Hernandez, and N. Tufenkji, "Microplastics and nanoplastics in aquatic environments: aggregation, deposition, and enhanced contaminant transport," *Environmental science & technology*, vol. 52, no. 4, pp. 1704-1724, 2018.
- [6] K. L. Law *et al.*, "Plastic accumulation in the North Atlantic subtropical gyre," *Science*, vol. 329, no. 5996, pp. 1185-1188, 2010.
- [7] Q. Deshoules, M. Le Gall, C. Dreanno, M. Arhant, D. Priour, and P. Le Gac, "Chemical coupling between oxidation and hydrolysis in polyamide 6-A key aspect in the understanding of microplastic formation," *Polymer Degradation and Stability*, vol. 197, p. 109851, 2022.
- [8] M. Arhant, M. Le Gall, P.-Y. Le Gac, and P. Davies, "Impact of hydrolytic degradation on mechanical properties of PET-Towards an understanding of microplastics formation," *Polymer degradation and stability*, vol. 161, pp. 175-182, 2019.
- [9] A. L. Andrady, "Microplastics in the marine environment," *Marine pollution bulletin*, vol. 62, no. 8, pp. 1596-1605, 2011.
- [10] D. Carlsson and D. Wiles, "The photooxidative degradation of polypropylene. Part I. Photooxidation and photoinitiation processes," *Journal of Macromolecular Science—Reviews in Macromolecular Chemistry*, vol. 14, no. 1, pp. 65-106, 1976.
- [11] D. Teare, N. Emmison, C. Ton-That, and R. Bradley, "Cellular attachment to ultraviolet ozone modified polystyrene surfaces," *Langmuir*, vol. 16, no. 6, pp. 2818-2824, 2000.
- [12] X.-F. Wei *et al.*, "Millions of microplastics released from a biodegradable polymer during biodegradation/enzymatic hydrolysis," *Water Research*, vol. 211, p. 118068, 2022.
- [13] A. R. Othman, H. A. Hasan, M. H. Muhamad, N. I. Ismail, and S. R. S. Abdullah, "Microbial degradation of microplastics by enzymatic processes: a review," *Environmental Chemistry Letters*, vol. 19, no. 4, pp. 3057-3073, 2021.
- [14] M. Cole, H. Webb, P. K. Lindeque, E. S. Fileman, C. Halsband, and T. S. Galloway, "Isolation of microplastics in biota-rich seawater samples and marine organisms," *Scientific reports*, vol. 4, no. 1, pp. 1-8, 2014.
- [15] S. Acharya, S. S. Rumi, Y. Hu, and N. Abidi, "Microfibers from synthetic textiles as a major source of microplastics in the environment: A review," *Textile*

- Research Journal*, vol. 91, no. 17-18, pp. 2136-2156, 2021.
- [16] P. Bhattacharya, "A review on the impacts of microplastic beads used in cosmetics," *Acta Biomed. Sci*, vol. 3, no. 4, 2016.
- [17] D. He, Y. Luo, S. Lu, M. Liu, Y. Song, and L. Lei, "Microplastics in soils: Analytical methods, pollution characteristics and ecological risks," *TrAC Trends in Analytical Chemistry*, vol. 109, pp. 163-172, 2018.
- [18] Q. A. T. Nguyen, H. N. Y. Nguyen, E. Strady, Q. T. Nguyen, and M. Trinh-Dang, "Characteristics of microplastics in shoreline sediments from a tropical and urbanized beach (Da Nang, Vietnam)," *Marine Pollution Bulletin*, vol. 161, p. 111768, 2020.
- [19] J. Li, H. Liu, and J. P. Chen, "Microplastics in freshwater systems: A review on occurrence, environmental effects, and methods for microplastics detection," *Water research*, vol. 137, pp. 362-374, 2018.
- [20] M. Cole *et al.*, "Microplastic ingestion by zooplankton," *Environmental science & technology*, vol. 47, no. 12, pp. 6646-6655, 2013.
- [21] P. M. Canniff and T. C. Hoang, "Microplastic ingestion by *Daphnia magna* and its enhancement on algal growth," *Science of the Total Environment*, vol. 633, pp. 500-507, 2018.
- [22] R. Saborowski, Š. Korez, S. Riesbeck, M. Weidung, U. Bickmeyer, and L. Gutow, "Shrimp and microplastics: A case study with the Atlantic ditch shrimp *Palaemon varians*," *Ecotoxicology and Environmental Safety*, vol. 234, p. 113394, 2022.
- [23] M. Smith, D. C. Love, C. M. Rochman, and R. A. Neff, "Microplastics in seafood and the implications for human health," *Current environmental health reports*, vol. 5, no. 3, pp. 375-386, 2018.
- [24] C. E. Talsness, A. J. Andrade, S. N. Kuriyama, J. A. Taylor, and F. S. Vom Saal, "Components of plastic: experimental studies in animals and relevance for human health," *Philosophical Transactions of the Royal Society B: Biological Sciences*, vol. 364, no. 1526, pp. 2079-2096, 2009.
- [25] D. Lithner, Å. Larsson, and G. Dave, "Environmental and health hazard ranking and assessment of plastic polymers based on chemical composition," *Science of the total environment*, vol. 409, no. 18, pp. 3309-3324, 2011.
- [26] L. Peng, D. Fu, H. Qi, C. Q. Lan, H. Yu, and C. Ge, "Micro- and nano-plastics in marine environment: Source, distribution and threats—A review," *Science of the total environment*, vol. 698, p. 134254, 2020.
- [27] E. L. Teuten *et al.*, "Transport and release of chemicals from plastics to the environment and to wildlife," *Philosophical transactions of the royal society B: biological sciences*, vol. 364, no. 1526, pp. 2027-2045, 2009.
- [28] G. Vandermeersch *et al.*, "Environmental contaminants of emerging concern in seafood—European database on contaminant levels," *Environmental Research*, vol. 143, pp. 29-45, 2015.
- [29] W. R. Waldman and M. C. Rillig, "Microplastic research should embrace the complexity of secondary particles," ed: *ACS Publications*, 2020.
- [30] S. Magni *et al.*, "The fate of microplastics in an Italian Wastewater Treatment Plant," *Science of the total environment*, vol. 652, pp. 602-610, 2019.
- [31] M. Cole, P. Lindeque, C. Halsband, and T. S. Galloway, "Microplastics as contaminants in the marine environment: a review," *Marine pollution bulletin*,

- vol. 62, no. 12, pp. 2588-2597, 2011.
- [32] H. Wijesekara *et al.*, "Trace element dynamics of biosolids-derived microbeads," *Chemosphere*, vol. 199, pp. 331-339, 2018.
- [33] L. Bradney *et al.*, "Particulate plastics as a vector for toxic trace-element uptake by aquatic and terrestrial organisms and human health risk," *Environment international*, vol. 131, p. 104937, 2019.
- [34] A. S. Tagg, M. Sapp, J. P. Harrison, and J. s. J. Ojeda, "Identification and quantification of microplastics in wastewater using focal plane array-based reflectance micro-FT-IR imaging," *Analytical chemistry*, vol. 87, no. 12, pp. 6032-6040, 2015.
- [35] E. R. Zettler, T. J. Mincer, and L. A. Amaral-Zettler, "Life in the "plastisphere": microbial communities on plastic marine debris," *Environmental science & technology*, vol. 47, no. 13, pp. 7137-7146, 2013.
- [36] M. Fischer and B. M. Scholz-Böttcher, "Simultaneous trace identification and quantification of common types of microplastics in environmental samples by pyrolysis-gas chromatography–mass spectrometry," *Environmental science & technology*, vol. 51, no. 9, pp. 5052-5060, 2017.
- [37] S. Mintenig, P. S. Bäumlein, A. Koelmans, S. Dekker, and A. Van Wezel, "Closing the gap between small and smaller: towards a framework to analyse nano-and microplastics in aqueous environmental samples," *Environmental Science: Nano*, vol. 5, no. 7, pp. 1640-1649, 2018.
- [38] E. Dümichen, P. Eisentraut, C. G. Bannick, A.-K. Barthel, R. Senz, and U. Braun, "Fast identification of microplastics in complex environmental samples by a thermal degradation method," *Chemosphere*, vol. 174, pp. 572-584, 2017.
- [39] E. Dümichen, U. Braun, R. Senz, G. Fabian, and H. Sturm, "Assessment of a new method for the analysis of decomposition gases of polymers by a combining thermogravimetric solid-phase extraction and thermal desorption gas chromatography mass spectrometry," *Journal of Chromatography A*, vol. 1354, pp. 117-128, 2014.
- [40] E. Dümichen *et al.*, "Analysis of polyethylene microplastics in environmental samples, using a thermal decomposition method," *Water research*, vol. 85, pp. 451-457, 2015.
- [41] P. Eisentraut *et al.*, "Two birds with one stone—fast and simultaneous analysis of microplastics: microparticles derived from thermoplastics and tire wear," *Environmental Science & Technology Letters*, vol. 5, no. 10, pp. 608-613, 2018.
- [42] M. Rodríguez Chialanza, I. Sierra, A. Pérez Parada, and L. Fornaro, "Identification and quantitation of semi-crystalline microplastics using image analysis and differential scanning calorimetry," *Environmental Science and Pollution Research*, vol. 25, no. 17, pp. 16767-16775, 2018.
- [43] N. P. Ivleva, A. C. Wiesheu, and R. Niessner, "Microplastic in aquatic ecosystems," *Angewandte Chemie International Edition*, vol. 56, no. 7, pp. 1720-1739, 2017.
- [44] M. G. J. Löder, M. Kuczera, S. Mintenig, C. Lorenz, and G. Gerdt, "Focal plane array detector-based micro-Fourier-transform infrared imaging for the analysis of microplastics in environmental samples," *Environmental Chemistry*, vol. 12, no. 5, pp. 563-581, 2015.
- [45] S. Huppertsberg and T. P. Knepper, "Instrumental analysis of microplastics—

- benefits and challenges," *Analytical and bioanalytical chemistry*, vol. 410, no. 25, pp. 6343-6352, 2018.
- [46] A. K  ppler *et al.*, "Analysis of environmental microplastics by vibrational microspectroscopy: FTIR, Raman or both?," *Analytical and bioanalytical chemistry*, vol. 408, no. 29, pp. 8377-8391, 2016.
- [47] L. Mai, L.-J. Bao, L. Shi, C. S. Wong, and E. Y. Zeng, "A review of methods for measuring microplastics in aquatic environments," *Environmental Science and Pollution Research*, vol. 25, no. 12, pp. 11319-11332, 2018.
- [48] J. Lee and K.-J. Chae, "A systematic protocol of microplastics analysis from their identification to quantification in water environment: A comprehensive review," *Journal of Hazardous Materials*, vol. 403, p. 124049, 2021.
- [49] Z. Sobhani, X. Zhang, C. Gibson, R. Naidu, M. Megharaj, and C. Fang, "Identification and visualisation of microplastics/nanoplastics by Raman imaging (i): Down to 100 nm," *Water research*, vol. 174, p. 115658, 2020.
- [50] D. Schymanski, C. Goldbeck, H.-U. Humpf, and P. F  rst, "Analysis of microplastics in water by micro-Raman spectroscopy: release of plastic particles from different packaging into mineral water," *Water research*, vol. 129, pp. 154-162, 2018.
- [51] R. Lenz, K. Enders, C. A. Stedmon, D. M. Mackenzie, and T. G. Nielsen, "A critical assessment of visual identification of marine microplastic using Raman spectroscopy for analysis improvement," *Marine Pollution Bulletin*, vol. 100, no. 1, pp. 82-91, 2015.
- [52] J. Lin, C. Zhang, M. Xu, Y. Yuan, and J. Yao, "Surface-enhanced Raman spectroscopic identification in fingerprints based on adhesive Au nanofilm," *RSC advances*, vol. 8, no. 43, pp. 24477-24484, 2018.
- [53] X. Xue *et al.*, "Tailored FTO/Ag/ZIF-8 structure as SERS substrate for ultrasensitive detection," *Spectrochimica Acta Part A: Molecular and Biomolecular Spectroscopy*, vol. 282, p. 121693, 2022.
- [54] T. Gong *et al.*, "Development of SERS tags for human diseases screening and detection," *Coordination Chemistry Reviews*, vol. 470, p. 214711, 2022.
- [55] M. E. Navarro-Segura, R. D. Rivera-Rangel, A. Arizmendi-Morquecho, I. L  pez, J. Alvarez-Quintana, and M. Sanchez-Dominguez, "Ultra-high sensitivity surface-enhanced Raman spectroscopy (SERS) substrates based on Au nanostructured hollow octahedra," *Applied Materials Today*, vol. 29, p. 101598, 2022.
- [56] G. Xu *et al.*, "Surface-enhanced Raman spectroscopy facilitates the detection of microplastics <1 μm in the environment," *Environmental Science & Technology*, vol. 54, no. 24, pp. 15594-15603, 2020.
- [57] L. Lv *et al.*, "In situ surface-enhanced Raman spectroscopy for detecting microplastics and nanoplastics in aquatic environments," *Science of The Total Environment*, vol. 728, p. 138449, 2020.
- [58] Q. T. L   *et al.*, "Nanostructured Raman substrates for the sensitive detection of submicrometer-sized plastic pollutants in water," *Journal of Hazardous Materials*, vol. 402, p. 123499, 2021.
- [59] J. Caldwell, P. Taladriz-Blanco, B. Rothen-Rutishauser, and A. Petri-Fink, "Detection of sub-micro- and nanoplastic particles on gold nanoparticle-based substrates through surface-enhanced Raman scattering (SERS) spectroscopy,"

- Nanomaterials*, vol. 11, no. 5, p. 1149, 2021.
- [60] L. Chang *et al.*, "Nanowell-enhanced Raman spectroscopy enables the visualization and quantification of nanoplastics in the environment," *Environmental Science: Nano*, vol. 9, no. 2, pp. 542-553, 2022.
- [61] Y. Jeon *et al.*, "Detection of nanoplastics based on surface-enhanced Raman scattering with silver nanowire arrays on regenerated cellulose films," *Carbohydrate Polymers*, vol. 272, p. 118470, 2021.
- [62] X.-L. Nie *et al.*, "Recognition of plastic nanoparticles using a single gold nanopore fabricated at the tip of a glass nanopipette," *Chemical Communications*, vol. 55, no. 45, pp. 6397-6400, 2019.
- [63] B. Sharma, R. R. Frontiera, A.-I. Henry, E. Ringe, and R. P. Van Duyne, "SERS: Materials, applications, and the future," *Materials today*, vol. 15, no. 1-2, pp. 16-25, 2012.
- [64] S. Nie and S. R. Emory, "Probing single molecules and single nanoparticles by surface-enhanced Raman scattering," *science*, vol. 275, no. 5303, pp. 1102-1106, 1997.
- [65] K. Kneipp *et al.*, "Single molecule detection using surface-enhanced Raman scattering (SERS)," *Physical review letters*, vol. 78, no. 9, p. 1667, 1997.
- [66] C.-H. Lee and J. K.-H. Fang, "The onset of surface-enhanced Raman scattering for single-particle detection of submicroplastics," *Journal of Environmental Sciences*, vol. 121, pp. 58-64, 2022.
- [67] J. Caldwell, P. Taladriz-Blanco, B. Rothen-Rutishauser, and A. Petri-Fink, "Detection of Sub-Micro- and Nanoplastic Particles on Gold Nanoparticle-Based Substrates through Surface-Enhanced Raman Scattering (SERS) Spectroscopy," (in eng), *Nanomaterials (Basel)*, vol. 11, no. 5, Apr 28 2021, doi: 10.3390/nano11051149.
- [68] Q. Yang *et al.*, "Identification of trace polystyrene nanoplastics down to 50 nm by the hyphenated method of filtration and surface-enhanced Raman spectroscopy based on silver nanowire membranes," *Environmental Science & Technology*, vol. 56, no. 15, pp. 10818-10828, 2022.
- [69] X.-X. Zhou, R. Liu, L.-T. Hao, and J.-F. Liu, "Identification of polystyrene nanoplastics using surface enhanced Raman spectroscopy," *Talanta*, vol. 221, p. 121552, 2021.
- [70] Y. Chen, A. K. Awasthi, F. Wei, Q. Tan, and J. Li, "Single-use plastics: Production, usage, disposal, and adverse impacts," *Science of the total environment*, vol. 752, p. 141772, 2021.
- [71] S. Ziajahromi, P. A. Neale, L. Rintoul, and F. D. Leusch, "Wastewater treatment plants as a pathway for microplastics: development of a new approach to sample wastewater-based microplastics," *Water research*, vol. 112, pp. 93-99, 2017.
- [72] C. G. Avio, S. Gorbi, and F. Regoli, "Plastics and microplastics in the oceans: from emerging pollutants to emerged threat," *Marine environmental research*, vol. 128, pp. 2-11, 2017.
- [73] R. Scalenghe, "Resource or waste? A perspective of plastics degradation in soil with a focus on end-of-life options," *Heliyon*, vol. 4, no. 12, p. e00941, 2018.
- [74] A. A. de Souza Machado *et al.*, "Impacts of microplastics on the soil biophysical environment," *Environmental science & technology*, vol. 52, no. 17, pp. 9656-9665, 2018.

- [75] I. E. Napper, A. Bakir, S. J. Rowland, and R. C. Thompson, "Characterisation, quantity and sorptive properties of microplastics extracted from cosmetics," *Marine Pollution Bulletin*, vol. 99, no. 1, pp. 178-185, 2015.
- [76] L. M. Hernandez, N. Yousefi, and N. Tufenkji, "Are there nanoplastics in your personal care products?," *Environmental Science & Technology Letters*, vol. 4, no. 7, pp. 280-285, 2017.
- [77] J. Y. Ljubimova and E. Holler, "Biocompatible nanopolymers: the next generation of breast cancer treatment?," *Nanomedicine*, vol. 7, no. 10, pp. 1467-1470, 2012.
- [78] M. A. Browne *et al.*, "Accumulation of microplastic on shorelines worldwide: sources and sinks," *Environmental science & technology*, vol. 45, no. 21, pp. 9175-9179, 2011.
- [79] I. E. Napper and R. C. Thompson, "Release of synthetic microplastic plastic fibres from domestic washing machines: Effects of fabric type and washing conditions," *Marine pollution bulletin*, vol. 112, no. 1-2, pp. 39-45, 2016.
- [80] B. Stephens, P. Azimi, Z. El Orch, and T. Ramos, "Ultrafine particle emissions from desktop 3D printers," *Atmospheric Environment*, vol. 79, pp. 334-339, 2013.
- [81] A. L. Andrady *et al.*, "Oxidation and fragmentation of plastics in a changing environment; from UV-radiation to biological degradation," *Science of The Total Environment*, vol. 851, p. 158022, 2022.
- [82] G. C. Vega, A. Gross, and M. Birkved, "The impacts of plastic products on air pollution-A simulation study for advanced life cycle inventories of plastics covering secondary microplastic production," *Sustainable Production and Consumption*, vol. 28, pp. 848-865, 2021.
- [83] J. Jansen, "Plastic failure through molecular degradation: multiple mechanisms can attack polymer chains—here's what can go wrong," *Plastics Engineering*, vol. 71, no. 1, pp. 34-39, 2015.
- [84] B. Gewert, M. M. Plassmann, and M. MacLeod, "Pathways for degradation of plastic polymers floating in the marine environment," *Environ Sci Process Impacts*, vol. 17, no. 9, pp. 1513-21, 2015.
- [85] A. L. Andrady, "Persistence of plastic litter in the oceans," pp. 57-72, 2015.
- [86] A. A. Shah, F. Hasan, A. Hameed, and S. Ahmed, "Biological degradation of plastics: a comprehensive review," *Biotechnology advances*, vol. 26, no. 3, pp. 246-265, 2008.
- [87] Y. Zheng, E. K. Yanful, and A. S. Bassi, "A review of plastic waste biodegradation," *Critical reviews in biotechnology*, vol. 25, no. 4, pp. 243-250, 2005.
- [88] R. Mohee and G. Unmar, "Determining biodegradability of plastic materials under controlled and natural composting environments," *Waste management*, vol. 27, no. 11, pp. 1486-1493, 2007.
- [89] M. Shimao, "Biodegradation of plastics," *Current opinion in biotechnology*, vol. 12, no. 3, pp. 242-247, 2001.
- [90] P. Garcia-Muñoz, D. Robert, A. M. Ruppert, and N. Keller, "Chapter 1 - Microplastics (MPs) and nanoplastics (NPs): Introduction," pp. 1-32, 2023.
- [91] T. Hüffer, A. Praetorius, S. Wagner, F. Von der Kammer, and T. Hofmann, "Microplastic exposure assessment in aquatic environments: learning from

- similarities and differences to engineered nanoparticles," pp. 2499-2507, 2017.
- [92] K. Tallec, "Impacts des nanoplastiques et microplastiques sur les premiers stades de vie (gamètes, embryons, larves) de l'huître creuse *Crassostrea gigas*," *Brest*, 2019.
- [93] T. Galloway *et al.*, "Science-based solutions to plastic pollution," *One Earth*, vol. 2, pp. 5-7, 2020.
- [94] W. Yang *et al.*, "The combined toxicity influence of microplastics and nonylphenol on microalgae *Chlorella pyrenoidosa*," *Ecotoxicology and environmental safety*, vol. 195, p. 110484, 2020.
- [95] M. Tunali, E. N. Uzoefuna, M. M. Tunali, and O. Yenigun, "Effect of microplastics and microplastic-metal combinations on growth and chlorophyll a concentration of *Chlorella vulgaris*," *Science of the Total Environment*, vol. 743, p. 140479, 2020.
- [96] W. Wang, H. Gao, S. Jin, R. Li, and G. Na, "The ecotoxicological effects of microplastics on aquatic food web, from primary producer to human: A review," *Ecotoxicology and environmental safety*, vol. 173, pp. 110-117, 2019.
- [97] Z. Dai *et al.*, "Occurrence of microplastics in the water column and sediment in an inland sea affected by intensive anthropogenic activities," *Environmental pollution*, vol. 242, pp. 1557-1565, 2018.
- [98] S. L. Wright, R. C. Thompson, and T. S. Galloway, "The physical impacts of microplastics on marine organisms: a review," *Environmental pollution*, vol. 178, pp. 483-492, 2013.
- [99] E. A. Calderon, P. Hansen, A. Rodríguez, M. Blettler, K. Syberg, and F. R. Khan, "Microplastics in the digestive tracts of four fish species from the Ciénaga Grande de Santa Marta Estuary in Colombia," *Water, Air, & Soil Pollution*, vol. 230, no. 11, pp. 1-9, 2019.
- [100] K. Jabeen *et al.*, "Effects of virgin microplastics on goldfish (*Carassius auratus*)," *Chemosphere*, vol. 213, pp. 323-332, 2018.
- [101] I. Durán and R. Beiras, "Acute water quality criteria for polycyclic aromatic hydrocarbons, pesticides, plastic additives, and 4-Nonylphenol in seawater," *Environmental Pollution*, vol. 224, pp. 384-391, 2017.
- [102] O. A. Alabi, K. I. Ologbonjaye, O. Awosolu, and O. E. Alalade, "Public and environmental health effects of plastic wastes disposal: a review," *J Toxicol Risk Assess*, vol. 5, pp. 1-13, 2019.
- [103] T. Kögel, Ø. Bjorøy, B. Toto, A. M. Bienfait, and M. Sanden, "Micro-and nanoplastic toxicity on aquatic life: Determining factors," *Science of the Total Environment*, vol. 709, p. 136050, 2020.
- [104] J. C. Prata, J. P. da Costa, I. Lopes, A. C. Duarte, and T. Rocha-Santos, "Environmental exposure to microplastics: An overview on possible human health effects," *Science of the total environment*, vol. 702, p. 134455, 2020.
- [105] A. Rahman, A. Sarkar, O. P. Yadav, G. Achari, and J. Slobodnik, "Potential human health risks due to environmental exposure to nano-and microplastics and knowledge gaps: a scoping review," *Science of the Total Environment*, vol. 757, p. 143872, 2021.
- [106] Y. Wang and H. Qian, "Phthalates and their impacts on human health," *Healthcare*, vol. 9, p. 603, 2021.
- [107] F. Ribeiro, J. W. O'Brien, T. Galloway, and K. V. Thomas, "Accumulation and

- fate of nano-and micro-plastics and associated contaminants in organisms," *TrAC Trends in analytical chemistry*, vol. 111, pp. 139-147, 2019.
- [108] A. Isobe, K. Uchida, T. Tokai, and S. Iwasaki, "East Asian seas: a hot spot of pelagic microplastics," *Marine pollution bulletin*, vol. 101, pp. 618-623, 2015.
- [109] F. Watteau, M.-F. Dignac, A. Bouchard, A. Revallier, and S. Houot, "Microplastic detection in soil amended with municipal solid waste composts as revealed by transmission electronic microscopy and pyrolysis/GC/MS," *Frontiers in Sustainable Food Systems*, vol. 2, p. 14, 2018.
- [110] M. Funck, A. Yildirim, C. Nickel, J. Schram, T. C. Schmidt, and J. Tuerk, "Identification of microplastics in wastewater after cascade filtration using Pyrolysis-GC-MS," *MethodsX*, vol. 7, p. 100778, 2020.
- [111] I. V. Kirstein *et al.*, "Drinking plastics?—Quantification and qualification of microplastics in drinking water distribution systems by μ FTIR and Py-GCMS," *Water research*, vol. 188, p. 116519, 2021.
- [112] S. Primpke, M. Fischer, C. Lorenz, G. Gerds, and B. M. Scholz-Böttcher, "Comparison of pyrolysis gas chromatography/mass spectrometry and hyperspectral FTIR imaging spectroscopy for the analysis of microplastics," *Analytical and bioanalytical chemistry*, vol. 412, no. 30, pp. 8283-8298, 2020.
- [113] A. Gomiero, K. B. Øysæd, T. Agustsson, N. van Hoytema, T. van Thiel, and F. Grati, "First record of characterization, concentration and distribution of microplastics in coastal sediments of an urban fjord in south west Norway using a thermal degradation method," *Chemosphere*, vol. 227, pp. 705-714, 2019.
- [114] C. Dibke, M. Fischer, and B. M. Scholz-Böttcher, "Microplastic mass concentrations and distribution in German bight waters by pyrolysis–gas chromatography–mass spectrometry/thermochemolysis reveal potential impact of marine coatings: do ships leave skid marks?," *Environmental science & technology*, vol. 55, no. 4, pp. 2285-2295, 2021.
- [115] A. Ceccarini *et al.*, "The hidden microplastics: new insights and figures from the thorough separation and characterization of microplastics and of their degradation byproducts in coastal sediments," *Environmental science & technology*, vol. 52, no. 10, pp. 5634-5643, 2018.
- [116] E. D. Okoffo *et al.*, "Identification and quantification of selected plastics in biosolids by pressurized liquid extraction combined with double-shot pyrolysis gas chromatography–mass spectrometry," *Science of the Total Environment*, vol. 715, p. 136924, 2020.
- [117] G. Dierkes, T. Lauschke, S. Becher, H. Schumacher, C. Földi, and T. Ternes, "Quantification of microplastics in environmental samples via pressurized liquid extraction and pyrolysis-gas chromatography," *Analytical and bioanalytical chemistry*, vol. 411, no. 26, pp. 6959-6968, 2019.
- [118] X.-x. Zhou, L.-t. Hao, H.-y.-z. Wang, Y.-j. Li, and J.-f. Liu, "Cloud-point extraction combined with thermal degradation for nanoplastic analysis using pyrolysis gas chromatography–mass spectrometry," *Analytical chemistry*, vol. 91, no. 3, pp. 1785-1790, 2018.
- [119] P. Doyen *et al.*, "Occurrence and identification of microplastics in beach sediments from the Hauts-de-France region," *Environmental Science and Pollution Research*, vol. 26, no. 27, pp. 28010-28021, 2019.
- [120] L. Hermabessiere *et al.*, "Optimization, performance, and application of a

- pyrolysis-GC/MS method for the identification of microplastics," *Analytical and bioanalytical chemistry*, vol. 410, no. 25, pp. 6663-6676, 2018.
- [121] A. Dehaut *et al.*, "Microplastics in seafood: Benchmark protocol for their extraction and characterization," *Environmental Pollution*, vol. 215, pp. 223-233, 2016.
- [122] E. Fries, J. H. Dekiff, J. Willmeyer, M.-T. Nuelle, M. Ebert, and D. Remy, "Identification of polymer types and additives in marine microplastic particles using pyrolysis-GC/MS and scanning electron microscopy," *Environmental science: processes & impacts*, vol. 15, no. 10, pp. 1949-1956, 2013.
- [123] J. H. Dekiff, D. Remy, J. Klasmeier, and E. Fries, "Occurrence and spatial distribution of microplastics in sediments from Norderney," *Environmental Pollution*, vol. 186, pp. 248-256, 2014.
- [124] U. Braun, M. Jekel, G. Gerdt, N. Ivleva, and J. Reiber, "Microplastics analytics: sampling, preparation and detection methods," *Research Focus* 2018.
- [125] S. Mintenig, P. S. Bauerlein, A. A. Koelmans, S. C. Dekker, and A. Van Wezel, "Closing the gap between small and smaller: towards a framework to analyse nano-and microplastics in aqueous environmental samples," *Environmental Science: Nano*, vol. 5, no. 7, pp. 1640-1649, 2018.
- [126] N. P. Ivleva, "Chemical analysis of microplastics and nanoplastics: Challenges, advanced methods, and perspectives," *Chemical Reviews*, vol. 121, no. 19, pp. 11886-11936, 2021.
- [127] E. Dumichen, P. Eisentraut, M. Celina, and U. Braun, "Automated thermal extraction-desorption gas chromatography mass spectrometry: A multifunctional tool for comprehensive characterization of polymers and their degradation products," *Journal of Chromatography A*, vol. 1592, pp. 133-142, 2019.
- [128] U. Braun, K. Altmann, D. Herper, M. Knefel, M. Bednarz, and C. G. Bannick, "Smart filters for the analysis of microplastic in beverages filled in plastic bottles," *Food Additives & Contaminants: Part A*, vol. 38, no. 4, pp. 691-700, 2021.
- [129] V. Castelvetro, A. Corti, A. Ceccarini, A. Petri, and V. Vinciguerra, "Nylon 6 and nylon 6, 6 micro-and nanoplastics: A first example of their accurate quantification, along with polyester (PET), in wastewater treatment plant sludges," *Journal of hazardous materials*, vol. 407, p. 124364, 2021.
- [130] S. Primpke *et al.*, "Critical assessment of analytical methods for the harmonized and cost-efficient analysis of microplastics," *Applied Spectroscopy*, vol. 74, no. 9, pp. 1012-1047, 2020.
- [131] M. Simon, N. van Alst, and J. Vollertsen, "Quantification of microplastic mass and removal rates at wastewater treatment plants applying Focal Plane Array (FPA)-based Fourier Transform Infrared (FT-IR) imaging," *Water research*, vol. 142, pp. 1-9, 2018.
- [132] E. M. Cunningham *et al.*, "High abundances of microplastic pollution in deep-sea sediments: evidence from Antarctica and the Southern Ocean," *Environmental Science & Technology*, vol. 54, no. 21, pp. 13661-13671, 2020.
- [133] C. Lorenz *et al.*, "Spatial distribution of microplastics in sediments and surface waters of the southern North Sea," *Environmental Pollution*, vol. 252, pp. 1719-1729, 2019.
- [134] M. Bergmann *et al.*, "High quantities of microplastic in Arctic deep-sea

- sediments from the Hausgarten observatory," *Environmental science & technology*, vol. 51, no. 19, pp. 11000-11010, 2017.
- [135] I. E. Napper *et al.*, "Reaching new heights in plastic pollution—preliminary findings of microplastics on Mount Everest," *One Earth*, vol. 3, no. 5, pp. 621-630, 2020.
- [136] S. Piehl, A. Leibner, M. G. Löder, R. Dris, C. Bogner, and C. Laforsch, "Identification and quantification of macro-and microplastics on an agricultural farmland," *Scientific reports*, vol. 8, no. 1, pp. 1-9, 2018.
- [137] M. Trainic *et al.*, "Airborne microplastic particles detected in the remote marine atmosphere," *Communications Earth & Environment*, vol. 1, no. 1, pp. 1-9, 2020.
- [138] A. I. Catarino, V. Macchia, W. G. Sanderson, R. C. Thompson, and T. B. Henry, "Low levels of microplastics (MP) in wild mussels indicate that MP ingestion by humans is minimal compared to exposure via household fibres fallout during a meal," *Environmental pollution*, vol. 237, pp. 675-684, 2018.
- [139] A. C. Johnson *et al.*, "Identification and quantification of microplastics in potable water and their sources within water treatment works in England and Wales," *Environmental Science & Technology*, vol. 54, no. 19, pp. 12326-12334, 2020.
- [140] E. N. Waddell, N. Lascelles, and J. L. Conkle, "Microplastic contamination in Corpus Christi Bay blue crabs, *Callinectes sapidus*," *Limnology and Oceanography Letters*, vol. 5, no. 1, pp. 92-102, 2020.
- [141] D. Yang, H. Shi, L. Li, J. Li, K. Jabeen, and P. Kolandhasamy, "Microplastic pollution in table salts from China," *Environmental science & technology*, vol. 49, no. 22, pp. 13622-13627, 2015.
- [142] J. Brandt *et al.*, "High-Throughput analyses of microplastic samples using Fourier transform infrared and Raman spectrometry," *Applied Spectroscopy*, vol. 74, no. 9, pp. 1185-1197, 2020.
- [143] R. Salzer and H. W. Siesler, "Infrared and Raman spectroscopic imaging," *John Wiley & Sons*, 2014.
- [144] L. Cabernard, L. Roscher, C. Lorenz, G. Gerdtts, and S. Primpke, "Comparison of Raman and Fourier transform infrared spectroscopy for the quantification of microplastics in the aquatic environment," *Environmental science & technology*, vol. 52, no. 22, pp. 13279-13288, 2018.
- [145] S. Primpke, P. Dias, and G. Gerdtts, "Automated identification and quantification of microfibrils and microplastics," *Analytical Methods*, vol. 11, no. 16, pp. 2138-2147, 2019.
- [146] S. Mintenig, M. Löder, S. Primpke, and G. Gerdtts, "Low numbers of microplastics detected in drinking water from ground water sources," *Science of the total environment*, vol. 648, pp. 631-635, 2019.
- [147] S. M. Mintenig, I. Int-Veen, M. G. Löder, S. Primpke, and G. Gerdtts, "Identification of microplastic in effluents of waste water treatment plants using focal plane array-based micro-Fourier-transform infrared imaging," *Water research*, vol. 108, pp. 365-372, 2017.
- [148] G. S. Bumbrah and R. M. Sharma, "Raman spectroscopy – Basic principle, instrumentation and selected applications for the characterization of drugs of abuse," *Egyptian Journal of Forensic Sciences*, vol. 6, no. 3, pp. 209-215, 2016.

- [149] R. Krishna, T. J. Unsworth, and R. Edge, "Raman spectroscopy and microscopy," *Reference Module in Materials Science and Materials Engineering*, 2016.
- [150] O. I. Olubiyi, F.-K. Lu, D. Calligaris, F. A. Jolesz, and N. Y. Agar, "Chapter 17 - Advances in molecular imaging for surgery," pp. 407-439, 2015.
- [151] C. B. Crawford and B. Quinn, "10 - Microplastic identification techniques," pp. 219-267, 2017.
- [152] J. M. Cameron *et al.*, "Chapter 10 - Vibrational spectroscopic analysis and quantification of proteins in human blood plasma and serum," pp. 269-314, 2020.
- [153] K. Kneipp, H. Kneipp, I. Itzkan, R. R. Dasari, and M. S. Feld, "Ultrasensitive chemical analysis by Raman spectroscopy," *Chemical reviews*, vol. 99, no. 10, pp. 2957-2976, 1999.
- [154] C. Fang, Z. Sobhani, X. Zhang, C. T. Gibson, Y. Tang, and R. Naidu, "Identification and visualisation of microplastics/ nanoplastics by Raman imaging (ii): Smaller than the diffraction limit of laser?," *Water Research*, vol. 183, p. 116046, 2020/09/15/ 2020, doi: <https://doi.org/10.1016/j.watres.2020.116046>.
- [155] R. Aroca, "Surface-enhanced vibrational spectroscopy," 2006.
- [156] S. Nie and S. R. Emory, "Probing Single Molecules and Single Nanoparticles by Surface-Enhanced Raman Scattering," *Science*, vol. 275, no. 5303, p. 1102, 1997, doi: 10.1126/science.275.5303.1102.
- [157] K. Ueno and H. Misawa, "Surface plasmon-enhanced photochemical reactions," *Journal of Photochemistry and Photobiology C: Photochemistry Reviews*, vol. 15, pp. 31-52, 2013.
- [158] N. G. Greeneltch, M. G. Blaber, G. C. Schatz, and R. P. Van Duyne, "Plasmon-sampled surface-enhanced Raman excitation spectroscopy on silver immobilized nanorod assemblies and optimization for near infrared (λ_{ex} = 1064 nm) studies," *The Journal of Physical Chemistry C*, vol. 117, no. 6, pp. 2554-2558, 2013.
- [159] X. X. Han, R. S. Rodriguez, C. L. Haynes, Y. Ozaki, and B. Zhao, "Surface-enhanced Raman spectroscopy," *Nature Reviews Methods Primers*, vol. 1, no. 1, p. 87, 2021.
- [160] C. L. Haynes and R. P. Van Duyne, "Plasmon-sampled surface-enhanced Raman excitation spectroscopy," *The Journal of Physical Chemistry B*, vol. 107, no. 30, pp. 7426-7433, 2003.
- [161] P. Z. El-Khoury, "Tip-enhanced raman scattering on both sides of the schrödinger equation," *Accounts of Chemical Research*, vol. 54, no. 24, pp. 4576-4583, 2021.
- [162] R. A. Alvarez-Puebla and L. M. Liz-Marzán, "SERS detection of small inorganic molecules and ions," *Angewandte Chemie International Edition*, vol. 51, no. 45, pp. 11214-11223, 2012.
- [163] A. I. Pérez-Jiménez, D. Lyu, Z. Lu, G. Liu, and B. Ren, "Surface-enhanced Raman spectroscopy: benefits, trade-offs and future developments," *Chemical science*, vol. 11, no. 18, pp. 4563-4577, 2020.
- [164] S. Cong *et al.*, "Noble metal-comparable SERS enhancement from semiconducting metal oxides by making oxygen vacancies," *Nature communications*, vol. 6, no. 1, p. 7800, 2015.

- [165] B. Yang *et al.*, "Recent development of SERS technology: Semiconductor-based study," *Acs Omega*, vol. 4, no. 23, pp. 20101-20108, 2019.
- [166] S. Cong *et al.*, "Electrochromic semiconductors as colorimetric SERS substrates with high reproducibility and renewability," *Nature communications*, vol. 10, no. 1, p. 678, 2019.
- [167] P. Mandal and B. Tewari, "Progress in surface enhanced Raman scattering molecular sensing: A review," *Surfaces and Interfaces*, vol. 28, p. 101655, 2022.
- [168] Z. Huang *et al.*, "Plasmon-tunable Au@ Ag core-shell spiky nanoparticles for surface-enhanced Raman scattering," *Nano Research*, vol. 12, no. 2, pp. 449-455, 2019.
- [169] G. Baffou, J. Polleux, H. Rigneault, and S. Monneret, "Super-heating and micro-bubble generation around plasmonic nanoparticles under cw illumination," *The Journal of Physical Chemistry C*, vol. 118, no. 9, pp. 4890-4898, 2014.
- [170] J. Liu, G. Xu, X. Ruan, K. Li, and L. Zhang, "V-shaped substrate for surface and volume enhanced Raman spectroscopic analysis of microplastics," *Frontiers of Environmental Science & Engineering*, vol. 16, no. 11, p. 143, 2022.
- [171] R. Hu, K. Zhang, W. Wang, L. Wei, and Y. Lai, "Quantitative and sensitive analysis of polystyrene nanoplastics down to 50 nm by surface-enhanced Raman spectroscopy in water," *Journal of Hazardous Materials*, vol. 429, p. 128388, 2022.
- [172] G. Li *et al.*, "Single-particle analysis of micro/nanoplastics by SEM-Raman technique," *Talanta*, vol. 249, p. 123701, 2022.
- [173] J. Li *et al.*, "Particle-in-molybdenum disulfide-coated cavity structure with a Raman internal standard for sensitive Raman detection of water contaminants from ions to <300 nm nanoplastics," *The Journal of Physical Chemistry Letters*, vol. 13, no. 25, pp. 5815-5823, 2022.
- [174] R. Yin *et al.*, "Sensitive and rapid detection of trace microplastics concentrated through Au-nanoparticle-decorated sponge on the basis of surface-enhanced Raman spectroscopy," *Environmental Advances*, vol. 5, p. 100096, 2021.
- [175] N. K. Mogha and D. Shin, "Nanoplastic detection with surface enhanced Raman spectroscopy: Present and future," *TrAC Trends in Analytical Chemistry*, vol. 158, p. 116885, 2023.
- [176] X. Yan, T. Suzuki, Y. Kitahama, H. Sato, T. Itoh, and Y. Ozaki, "A study on the interaction of single-walled carbon nanotubes (SWCNTs) and polystyrene (PS) at the interface in SWCNT-PS nanocomposites using tip-enhanced Raman spectroscopy," *Physical Chemistry Chemical Physics*, vol. 15, no. 47, pp. 20618-20624, 2013.
- [177] T. E. Bridges, M. P. Houlne, and J. M. Harris, "Spatially Resolved Analysis of Small Particles by Confocal Raman Microscopy: Depth Profiling and Optical Trapping," *Analytical Chemistry*, vol. 76, no. 3, pp. 576-584, 2004.
- [178] Z. Sobhani, M. Al Amin, R. Naidu, M. Megharaj, and C. Fang, "Identification and visualisation of microplastics by Raman mapping," *Analytica Chimica Acta*, vol. 1077, pp. 191-199, 2019.
- [179] J. T. Wen, C. M. Ho, and P. B. Lillehoj, "Coffee ring aptasensor for rapid protein detection," (in eng), *Langmuir*, vol. 29, no. 26, pp. 8440-6, 2013.
- [180] Y. Liu, C. Z. Huang, and Y. F. Li, "Fluorescence assay based on preconcentration by a self-ordered ring using berberine as a model analyte," (in

- eng), *Anal Chem*, vol. 74, no. 21, pp. 5564-8, 2002.
- [181] T. S. Wong, T. H. Chen, X. Shen, and C. M. Ho, "Nanochromatography driven by the coffee ring effect," (in eng), *Anal Chem*, vol. 83, no. 6, pp. 1871-3, 2011.
- [182] S.-Y. Ding, E.-M. You, Z.-Q. Tian, and M. Moskovits, "Electromagnetic theories of surface-enhanced Raman spectroscopy," *Chemical Society Reviews*, vol. 46, no. 13, pp. 4042-4076, 2017.





จุฬาลงกรณ์มหาวิทยาลัย
CHULALONGKORN UNIVERSITY

VITA

NAME Boonphop Chaisrikhwun

DATE OF BIRTH 19 Jan 1993

PLACE OF BIRTH Yala

INSTITUTIONS ATTENDED 2015 B.Sc. Chemistry for Industry, Prince of Songkla University, Surat Thani Campus, Surat Thani, Thailand
2019 M.Sc. Rubber Technology, Prince of Songkla University, Surat Thani Campus, Surat Thani, Thailand

HOME ADDRESS 23 Moo 6 Tambon Khao Daeng, Amphoe Saba Yoi, Chang Wat Songkhla, 90210 Thailand

PUBLICATION Chaisrikhwun, B., Ekgasit, S., & Pienpinijtham, P. (2023). Size-independent quantification of nanoplastics in various aqueous media using surfaced-enhanced Raman scattering. *Journal of Hazardous Materials*, 442, 130046.